

Synthesis of thin film infinite-layer nickelates by atomic hydrogen reduction: Clarifying the role of the capping layer

Cite as: APL Mater. 12, 031132 (2024); doi: 10.1063/5.0197304

Submitted: 12 January 2024 • Accepted: 7 March 2024 •

Published Online: 25 March 2024








View Online



Export Citation



CrossMark

C. T. Parzyck,¹  V. Anil,¹  Y. Wu,¹  B. H. Goodge,^{2,3}  M. Roddy,¹  L. F. Kourkoutis,^{2,3} 
D. G. Schlom,^{3,4,5}  and K. M. Shen^{1,3,6,a)} 

AFFILIATIONS

¹Laboratory of Atomic and Solid State Physics, Department of Physics, Cornell University, Ithaca, New York 14853, USA

²School of Applied and Engineering Physics, Cornell University, Ithaca, New York 14853, USA

³Kavli Institute at Cornell for Nanoscale Science, Cornell University, Ithaca, New York 14853, USA

⁴Department of Materials Science and Engineering, Cornell University, Ithaca, New York 14853, USA

⁵Leibniz-Institut für Kristallzüchtung, Max-Born-Straße 2, 12489 Berlin, Germany

⁶Institut de Ciència de Materials de Barcelona (ICMAB-CSIC), Campus UAB, Bellaterra 08193, Spain

^{a)} Author to whom correspondence should be addressed: kmschen@cornell.edu

ABSTRACT

We present an integrated procedure for the synthesis of infinite-layer nickelates using molecular-beam epitaxy with gas-phase reduction by atomic hydrogen. We first discuss challenges in the growth and characterization of perovskite NdNiO₃/SrTiO₃, arising from post growth crack formation in stoichiometric films. We then detail a procedure for fully reducing NdNiO₃ films to the infinite-layer phase, NdNiO₂, using atomic hydrogen; the resulting films display excellent structural quality, smooth surfaces, and lower residual resistivities than films reduced by other methods. We utilize the *in situ* nature of this technique to investigate the role that SrTiO₃ capping layers play in the reduction process, illustrating their importance in preventing the formation of secondary phases at the exposed nickelate surface. A comparative bulk- and surface-sensitive study indicates that the formation of a polycrystalline crust on the film surface serves to limit the reduction process.

© 2024 Author(s). All article content, except where otherwise noted, is licensed under a Creative Commons Attribution (CC BY) license (<http://creativecommons.org/licenses/by/4.0/>). <https://doi.org/10.1063/5.0197304>

I. INTRODUCTION

Over the past four years, there has been a renewed interest in the synthesis of rare-earth perovskite and infinite-layer (IL) nickelates, spurred on by the discovery of superconductivity in the IL nickelates.^{1–4} Owing to challenging synthesis conditions for nickelate single crystals^{5,6} and their subsequent reduction to the IL phase,^{7–11} much of this work has focused on thin films; to date, superconductivity has not yet been observed in bulk, reduced nickelates. Correspondingly, there has been a recent renaissance in the study of perovskite nickelates, their metal-to-insulator transition (MIT),¹² and accompanying antiferromagnetism.^{13,14} Nonetheless, the growth and reduction of NdNiO₃ thin films are not with-

out their own challenges. Non-stoichiometry^{15–18} and strain^{19–21} both substantially influence the growth and properties of the precursor phase, as well as the quality of subsequently reduced films.²² Furthermore, the typical calcium hydride reduction process employed to form the IL phase typically reduces sample crystallinity, with weaker diffraction peaks observed in reduced films than in their precursors. This degradation is at least partially attributable to the instability of Ni¹⁺ in the IL phase, which decomposes into the thermodynamically preferred 2+ state at elevated temperatures.^{23,24} As a result, long reaction times (typically hours for films and days in bulk) induce competition between reduction and decomposition during the low-temperature second step.

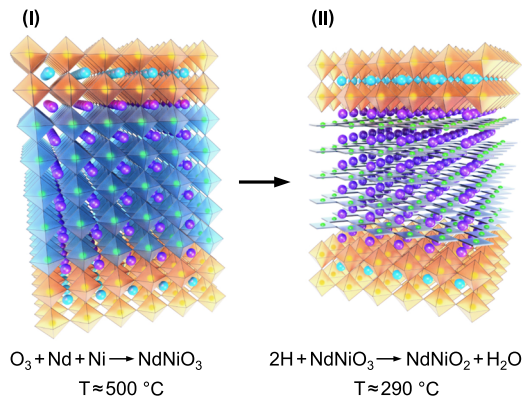


FIG. 1. Schematic of the two-step *in situ* synthesis of $NdNiO_2$. (I) First, the perovskite $NdNiO_3$ film is grown using distilled ozone and molecular beams of Nd and Ni. (II) Second, the temperature is lowered and atomic hydrogen is flowed across the sample surface, scavenging oxygen from the film and topotactically reducing it to $NdNiO_2$. H_2O generated from this reaction is removed from the system with a high-vacuum pump.

In this article, we discuss the *in situ* synthesis of $NdNiO_2$ thin films using a combined molecular-beam epitaxy and atomic hydrogen reduction system. We begin with a description of some obstacles to the growth of thin films of $NdNiO_3$ under high tensile strain ($\epsilon = 2.6\%$) on (001) $SrTiO_3$ substrates, including the confounding factors of non-stoichiometry and strain relaxation on the transport properties of precursor films. We identify a strong aging effect in the resistivity of stoichiometric films and, using a combination of x-ray diffraction (XRD) and high-resolution scanning transmission electron microscopy (STEM), demonstrate it results from post-growth strain relaxation via the formation of microscopic cracks. After identifying suitable conditions for the growth of the perovskite, we introduce a novel procedure for reduction to the IL phase using an atomic-hydrogen-beam source (Fig. 1).^{25,26} We show that topotactic reduction of $NdNiO_3$ to $NdNiO_2$ utilizing atomic hydrogen can be accomplished in short periods (<20 min) and without the need to remove the films from the vacuum. Structural and electrical transport measurements indicate a high degree of crystallinity and low surface roughness, establishing this method as a viable alternative to traditional direct contact reduction procedures. The amenability of this technique to integration with surface sensitive probes is demonstrated by studying the reduction process using reflection high-energy electron diffraction (RHEED). The ability to perform surface-sensitive diffraction allows us to investigate the importance of $SrTiO_3$ capping layers on the reduction of nickelate films, illustrating that uncapped films suffer degradation of the film surface during the reduction. Furthermore, comparisons between bulk and surface sensitive measurements indicate that the formation of this secondary-phase “crust” strongly impacts the reduction process; the same reduction conditions that produce the IL phase in capped samples are insufficient to significantly reduce comparable uncapped samples. The fact that the addition of a single $SrTiO_3$ cap layer to a 20 u.c. thick film drastically changes the reduction rate of the whole film suggests that the primary importance of the capping layer is, counterintuitively, to facilitate oxygen removal from the system.

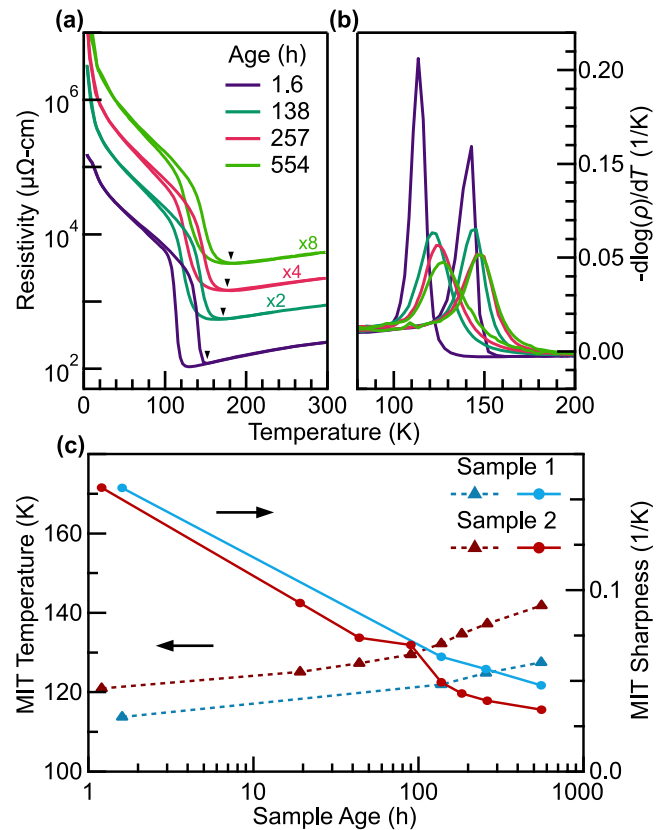


FIG. 2. Aging effects on the electrical transport properties of 20 u.c. thick $NdNiO_3$ films on $SrTiO_3$. (a) Resistivity of a 20 u.c. film measured repeatedly after its initial growth; traces have been offset for clarity. (b) Logarithmic derivative of the data from panel (a). (c) Transition sharpness and temperature, the maximum value and location of the logarithmic derivative of the resistivity, respectively, for two nominally identical samples measured at different time intervals following growth.

II. SYNTHESIS OF THE PEROVSKITE PRECURSOR

Historically, nickelate thin films have been synthesized using a wide variety of techniques, including pulsed-laser deposition,²⁷ off-axis magnetron sputtering,¹² and molecular-beam epitaxy (MBE);²⁸ in all cases, the perovskite exhibits a strong sensitivity to composition, both in terms of the cation ratio^{15–17} and oxygen non-stoichiometry.^{19,20} We utilize reactive oxide MBE with distilled ozone (~80%) as the oxidizing agent and a shuttered growth strategy with initial shutter times calibrated using RHEED oscillation measurements of NiO and Nd_2O_3 ²⁹ and refined using the method described by Li *et al.*¹⁸ The film composition is inferred from the out-of-plane lattice constant, which has a measurable dependence on the cation ratio to the percent level (*c.f.* the supplementary material). Following this procedure, we obtain a minimal out-of-plane lattice constant of 3.736 Å from Nelson–Riley analysis³⁰ and fully coherent films with sharp MITs. It has been shown previously that the strength and sharpness of the MIT are strongly influenced by the film non-stoichiometry;^{16,17,31} in our films, we do observe a dependence of the MIT sharpness on the cation

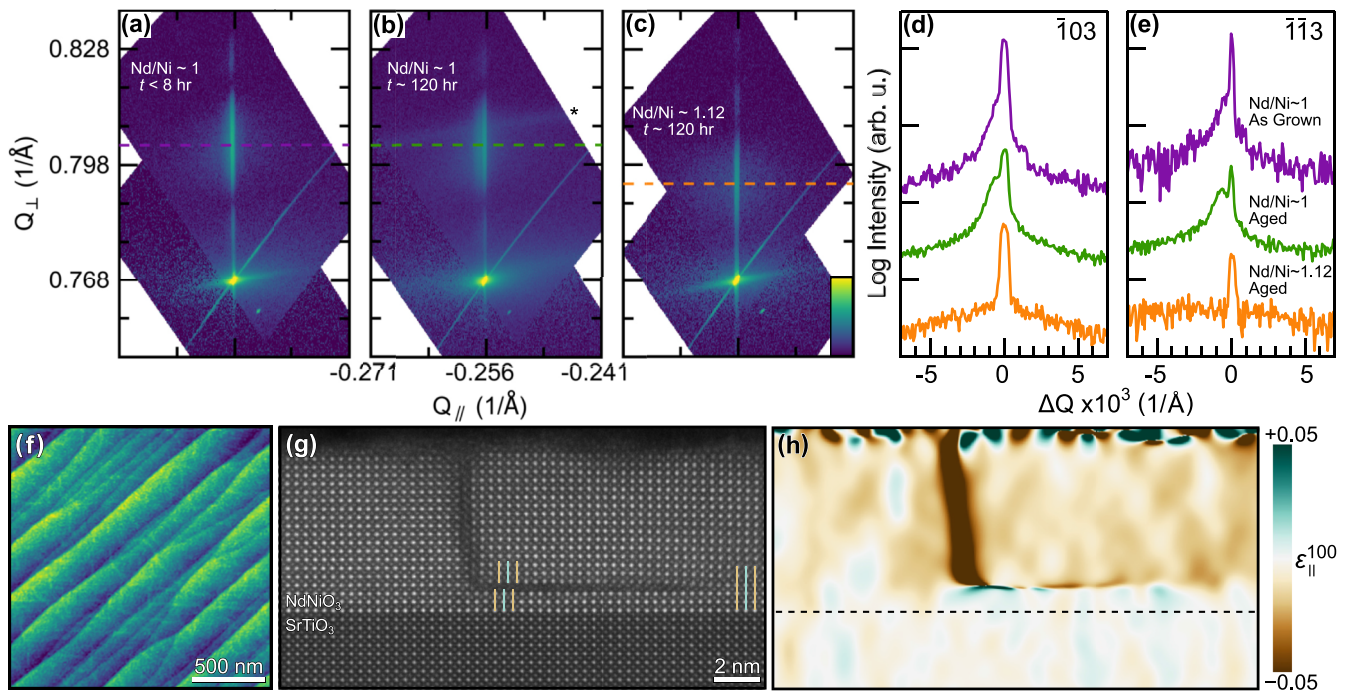


FIG. 3. Aging effects on the structure of 20 u.c. thick NdNiO_3 films on SrTiO_3 . (a) Reciprocal space map about the $\bar{1}03$ peaks of a stoichiometric film measured at a time $t < 8$ hours after growth. (b) Measurement of the same sample ~ 120 h later; (*) polycrystalline ring from residual silver paint on sample edge. (c) Measurement of a non-stoichiometric film ($\text{Nd/Ni} \approx 1.12$) 5 days following growth. (d) Line cuts from panels (a)–(c) at the peak maximum $\pm 2 \times 10^{-3} \text{ \AA}^{-1}$, traces offset for clarity. (e) Line cuts from equivalent positions on maps about the $\bar{1}13$ peaks of the same films. (f) AFM image of an aged (>1 week) NdNiO_3 sample showing striations. (g) High-angle annular dark-field image of a crack and resulting delamination in a 3-day-old sample; lines highlight columns of Nd atoms, which should be continuous. (h) Map of in-plane compressive strain in (g), highlighting local changes in the lattice fringe spacing.

ratio but do not realize a complete suppression of the MIT in the neodymium rich limit (as observed in films under compressive strain^{16,31}). A comparison of the film resistivity and MIT transition temperature shows monotonic dependence on the lattice constant, further evidencing it as a good metric for the film non-stoichiometry.

A. Resistivity of the perovskite

Having tuned the cation ratio to nearly 1-to-1, we investigate the electrical properties of the resulting films. When the resistivity of a 20 pseudocubic (pc) unit cell (u.c.) film is measured within 2 h following growth; Fig. 2(a), the MIT is sharp, with an upturn in the cooling curve at ~ 140 K followed by a hysteretic return in the warming curve at ~ 159 K. When the measurement is repeated, however, ~ 6 days later, the hysteresis loop is noticeably broadened, and these two temperatures are nearly coincident at an elevated value of ~ 170 K. Subsequent measurements show further widening of the transition, an increase in the upturn temperature to >180 K, and an increase in the room temperature resistivity. The maximum value of the logarithmic derivative of the resistivity, $(-d \log(\rho)/dT)$, gives a measure of the MIT sharpness, and its position provides an even-handed measurement of the transition temperature. Corresponding curves of the logarithmic derivatives and extracted values

are shown in Figs. 2(b) and 2(c); the MIT sharpness (temperature) monotonically decreases (increases) roughly logarithmically with time. A second, nominally identical, sample was measured over the same time period but at a greater frequency and showed identical trends in the sharpness and transition temperatures, verifying that the observed effect is time-dependent rather than a by-product of thermal cycling (both samples were stored in a N_2 purged desiccator between measurements). While the degradation of films under such high tensile strain is not wholly unexpected, the substantial changes in the electrical properties over the course of a single day could confound (epitaxial) strain studies of the MIT in the perovskite nickelates.

B. Post-growth structural relaxation

In Fig. 3, we show that the observed changes in resistivity are attributable to post growth strain relaxation by way of crack formation. A reciprocal space map (RSM) about the $\bar{1}03$ pc reflection of a stoichiometric film, measured immediately following growth, shows a sharp peak aligned with the substrate; upon repetition of the measurement 5 days later, a significant shoulder is apparent. When a purposefully neodymium rich film ($\text{Nd:Ni} \sim 1.12$) is measured 5 days following growth, however, no shoulder is observed, indicating the film remains coherent. This, and equivalent data about

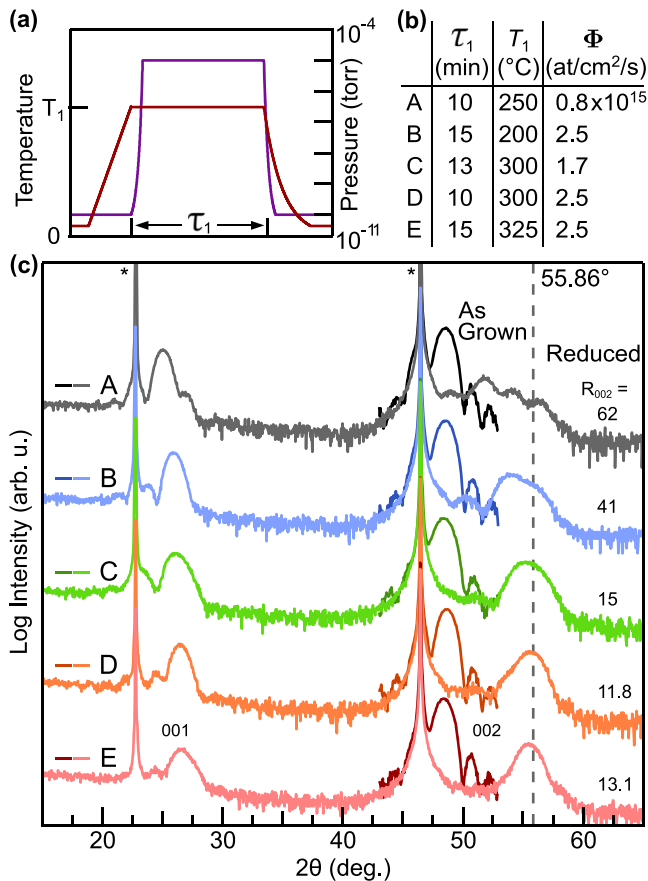


FIG. 4. Single temperature topotactic reduction of $\text{NdNiO}_3/\text{SrTiO}_3$ with atomic hydrogen. (a) Schematic of the reduction procedure at a single temperature T_1 for a duration τ_1 . (b) Time, temperature, and flux conditions for the reduction of samples shown in (c). (c) X-ray diffraction of a series of samples before (dark) and after (light) reduction, offset for clarity. The ratio of the 002 peak height, R_{002} , before and after reduction signifies the retention of crystallinity through the process, with smaller numbers indicating better quality of the reduced film. All samples were capped with 1–3 layers of SrTiO_3 . (*) indicates reflections arising from the SrTiO_3 substrate.

$(\overline{113})_{\text{pc}}$ summarized in Figs. 3(d) and 3(e), are consistent with fully coherent as-grown films, regardless of the cation non-stoichiometry. Nonetheless, films with $\text{Nd:Ni} \sim 1$ do not maintain coherence on the hour timescale. Instead, they form regions with a smaller in-plane lattice parameter: $a_{\text{pc}} \sim 3.891(5)$ —intermediate to the substrate (3.905 Å), and bulk³² (3.807 Å) parameters. Partial relaxation toward the bulk-like structure explains the time dependent increase in the MIT temperature toward that of the bulk compound. The fact that neodymium-rich films do not form relaxed regions suggests that the presence of Ruddlesden–Popper (RP) faults, identified in Nd rich films,²² contributes to the accommodation of both off-stoichiometry as well as high tensile strain.

Real-space probes, including atomic force microscopy (AFM) and STEM, reveal relaxation in the film is accomplished by crack formation and subsequent partial delamination. AFM of an aged,

stoichiometric film, Fig. 3(f), shows terraces decorated with raised striations running along and across the step edges, indicative of cracking and subsequent delamination, as observed prior in perovskite oxides under biaxial tensile strain.³³ This partial delamination is directly visible by atomic-resolution HAADF-STEM imaging in Fig. 3(g), where the top surface of the film is slightly raised on one side of the crack's vertical extension. In addition to the vertical lifting of the atomic layers, in-plane relaxation above the crack can be identified by Nd atomic columns, which are offset above and below the horizontal extension (cyan and yellow lines) and by a small effective compression of the in-plane lattice fringe spacing³⁴ (light brown) in Fig. 3(h). In addition to the aforementioned time dependence in electrical transport caused by partial relaxation, the formation of extended defects may present a challenge to the reproducibility of reduction experiments. If the time between growth and reduction is not controlled, as the off-stoichiometry of the parent phase is reduced and the frequency of RP faults diminishes, the quality of the corresponding reduced films may become difficult to predict.

III. REDUCTION TO INFINITE-LAYER NdNiO_2

Having established conditions for the synthesis of the perovskite, we introduce a novel reduction procedure to transform it into the infinite-layer phase. Traditionally, low-temperature topotactic reduction of nickelates utilizes alkali or alkaline earth hydride powders (CaH_2 , NaH) as reducing agents. This process was introduced in studies of intermixed polycrystalline samples,^{23,24,35,36} later applied to films,^{37–39} and most recently refined for the production of superconducting alkaline-earth (AE) doped rare-earth (RE) nickelates, $(\text{RE},\text{AE})\text{NiO}_2$.^{1,2,22,40–42} Despite the success of this method, there are a few drawbacks. Primarily, it is limited to *ex situ* use—the film needs to be removed from the growth chamber and placed in an environment with the powder, annealed, and then the reaction products removed. Often, the sample is embedded in the powder⁴³ (although there have been reports of non-contact reduction^{7,44,45}), which is not amenable to surface sensitive measurements, including scanning tunneling microscopy and photoemission spectroscopy. These techniques, fundamental to understanding the cuprates, remain uncommon in the infinite-layer nickelates.^{46–48} In addition, long reduction times (typically hours for thin films and days for single crystals) may be detrimental to the preservation of crystallinity, as bulk studies indicate extended exposure to temperatures exceeding 200 °C results in decomposition or disproportionation of the metastable structure.^{8,23,24} We note that there has been a recent push to identify new reduction methods for nickelates, and reduction by application of an aluminum getter layer to the film surface has been recently demonstrated.^{49,50} Similar to the recently identified solid-state aluminum reduction technique, the method described here can be achieved in the same vacuum system as the sample growth.

The use of atomic hydrogen as a powerful reducing agent has been recognized previously;⁵¹ however, to date, its use has primarily been consigned to surface etching⁵² and cleaning,^{53,54} with some work on the reduction of binary oxides^{55–57} or the generation of oxygen vacancies in more complex oxides.⁵⁸ We find that exposure to an atomic hydrogen flux of $\sim 2 \times 10^{15}$ at./cm²/s for <15 min at sample temperatures between 250 and 300 °C is sufficient to transform ~ 7.5

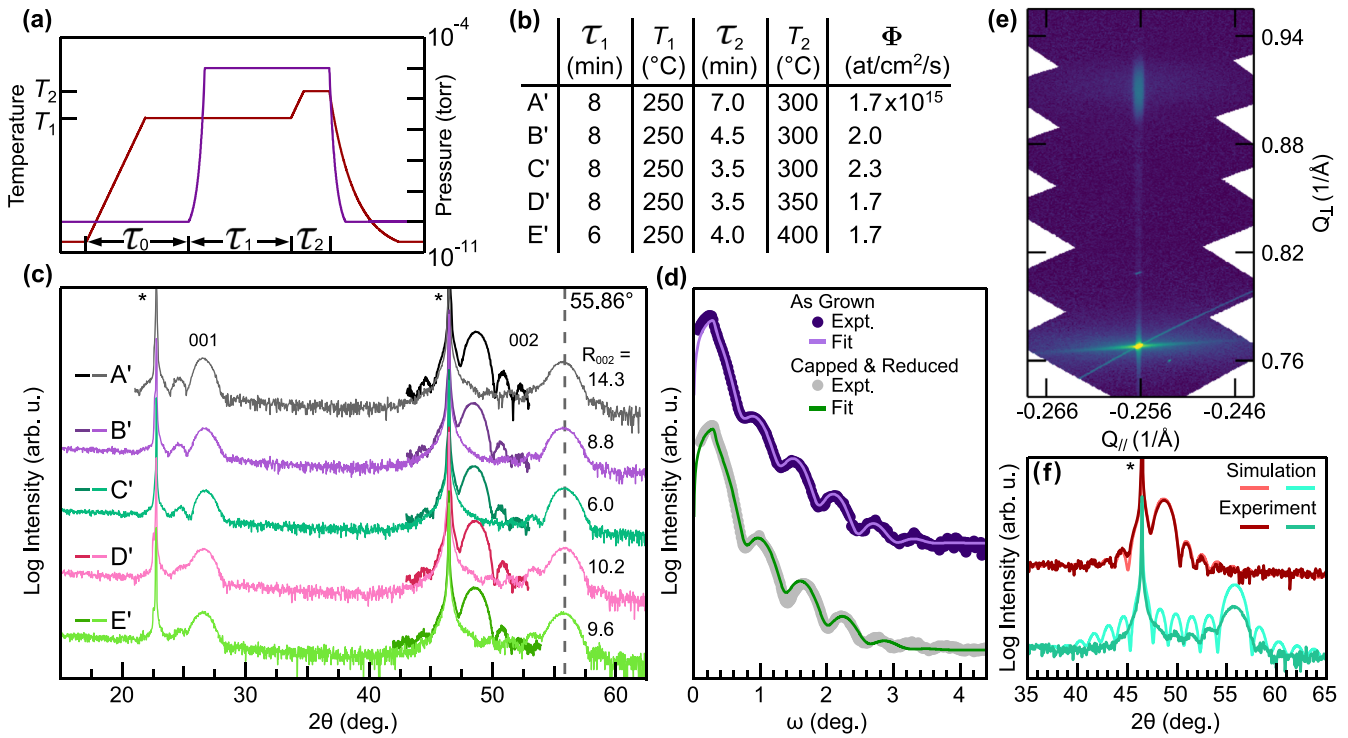


FIG. 5. Structural characterization of optimally reduced NdNiO₂/SrTiO₃. (a) Schematic of the three-step reduction procedure. (b) Parameters used in the reduction of samples in (c); in all the pictured cases, an initial equilibration time of $\tau_0 = 8$ min was used. (c) XRD of samples before (dark) and after (light) reduction. The ratio of the 002 peak height before and after reduction ($R_{002} = I(2\theta = 48.71^\circ)/I'(2\theta = 55.86^\circ)$) is provided as a measure of the preservation of crystallinity during the reduction; smaller numbers indicate better preservation, with a theoretically ideal value of 1.58. (d) X-ray reflectivity of the same sample immediately after growth (black) and after capping with 2 u.c. of SrTiO₃ and reduction using the optimal conditions of C'. (e) Reciprocal space map about the $\bar{1}03$ peaks of SrTiO₃ and NdNiO₂ for a sample reduced under the optimized conditions. (f) XRD, about the 002 reflections of representative, optimized NdNiO₃ and NdNiO₂ films with simulated diffraction patterns overlaid. (*) indicates reflections arising from the SrTiO₃ substrate.

nm thick perovskite films to the IL phase, a much shorter exposure compared to traditional CaH₂ annealing.⁵⁹ We further demonstrate that this procedure produces IL films with high structural quality, smooth surfaces, and favorable electrical characteristics. Finally, we leverage the compatibility of this technique with *in situ* probes, namely, RHEED, to study the effects of atomic and molecular hydrogen exposure on the film surface and the resulting impact on the reduction process.

A. Single temperature reduction

Following growth, 20 u.c. thick nickelate films are capped with 2–3 unit cells of SrTiO₃ and transferred, in an ultra-high vacuum, to a connected chamber ($P_{\text{base}} < 1 \times 10^{-10}$ Torr) with a heated sample stage. There, atomic hydrogen is generated from a thermal source^{25,26} by passing molecular H₂ through a heated tungsten capillary (>1900 °C) located 9 cm from the sample. It dissociates (with an efficiency, α , between 50% and 80%)⁶⁰ before interacting with the sample surface, scavenging O₂ from the film, and forming H₂O,

which is removed via a turbomolecular pump. A schematic of a single-temperature reduction program, with typical parameters, is shown in Figs. 4(a) and 4(b); lab-based XRD measurements before and after reduction are detailed in Fig. 4(c). At low reaction times, temperatures, and fluxes (samples A, B), the perovskite transforms partially to the IL phase with a pair of additional intermediate peaks visible at $2\theta = 51.8^\circ$ ($c \sim 3.53$ Å) and $2\theta = 54.0^\circ$ ($c \sim 3.39$ Å), attributable to oxygen-deficient perovskite phases with partially collapsed structures. As the reaction temperature is increased from 250 to ~ 300 °C and the flux from < 1 to 2.5×10^{15} at./cm²/s (by varying the capillary temperature and H₂ flow rate), the intermediate phase peaks are suppressed in favor of a single peak above $2\theta = 55^\circ$, indicative of the IL phase (sample E). Eliminating these oxygen-rich phases from NdNiO₂ samples is of paramount importance to studies targeted at understanding the parent state from which superconductivity emerges. Excess interstitial oxygen tends to form ordered structures in all members of the RENiO₂, RE = La, Pr, Nd, family.^{11,61–67} Inclusions of these phases may serve to confound resonant scattering studies, which are highly sensitive to periodic valence modulations of nickel.⁶⁸

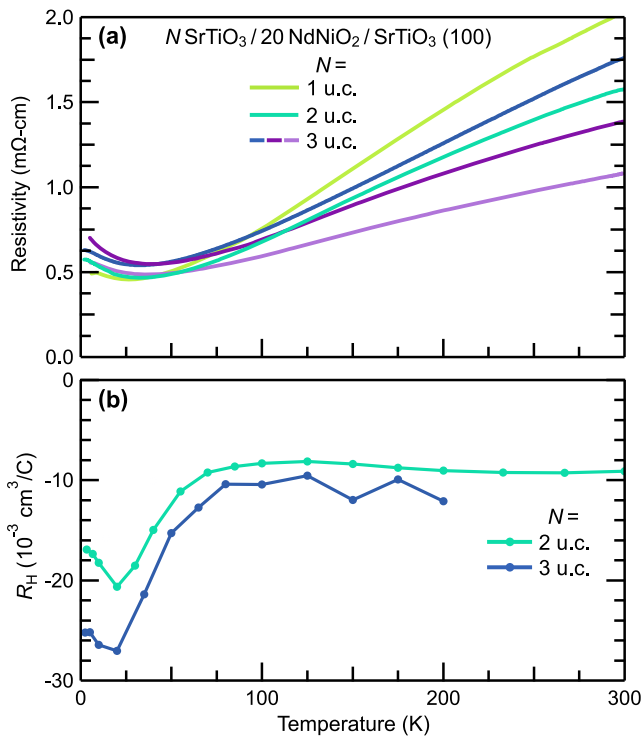


FIG. 6. Electrical transport measurements of reduced nickelate films. (a) Resistivity of representative reduced films with different SrTiO₃ cap thicknesses, N , reduced using the optimized three-step procedure. (b) Hall measurements of NdNiO₂ films capped with 2 or 3 u.c. SrTiO₃.

B. Three-step reduction

While the single temperature reduction procedure is shown to effectively produce the IL phase, the resulting films have reduced crystallinity compared to the perovskite, as evidenced by the reduction in the 002 Bragg peak intensity. We quantify the preservation of crystallinity during the transformation from the perovskite to the IL phase by the ratio of the 002 peak height before (I) and after (I') reduction: $R_{002} = I(2\theta = 48.71^\circ)/I'(2\theta = 55.86^\circ)$. Owing to changes in the structure factor, some decrease in intensity is expected: the optimal (i.e., minimal) value of R_{002} is calculated to be 1.58 using a dynamical diffraction model.⁶⁹ For reference, the value of R_{002} for sample E in Fig. 4(b) is 13.1. This discrepancy highlights that although the reduction proceeds across the entire thickness of the film (evidenced by the Scherrer thickness from the 002 peak), the process generates substantial densities of point and/or extended defects in the film and shrinks the domain sizes of coherent, crystalline material.

To further improve the crystallinity, we perform a three-step reduction procedure utilizing the independent control of the sample temperature and reducing atmosphere afforded in this setup. Outlined in Figs. 5(a) and 5(b), the procedure consists of (1) heating close to the reduction temperature ($\sim 250^\circ\text{C}$) in vacuum for 8 min to achieve thermal equilibrium; (2) the hydrogen flow is turned on and the sample exposed to the atomic H beam for 6–8 min as the flow rate stabilizes; and (3) the sample is quickly heated to the

final temperature for a short period, typically 3–5 min, before terminating the hydrogen flow and cooling the sample. As illustrated in the corresponding XRD measurements in Fig. 5(c), using similar parameters to those in Fig. 4 results in similar values of R_{002} (sample A'). Lowering the reduction time while increasing the temperature and flux appears to improve the retention of crystallinity, with full reduction achievable in only 10–12 min of total exposure time (samples C'–E'), with an optimized value of $R_{002} \approx 6$ in sample C'. The precise value of the high-temperature step does not appear to strongly influence R_{002} ; this is possibly attributable to the short duration of the final step, during which the sample surface may not fully equilibrate with the heater. Although the conditions of sample C' appear optimal, Fig. 5(b) illustrates that the IL phase can be isolated over a reasonable window of times, temperatures, and fluxes.

Further structural characterization is outlined in Figs. 5(d)–5(f). X-ray reflectivity (XRR) of a film is measured immediately after growth and then again following capping with 2 u.c. of SrTiO₃ and reduction. The thickness and roughness of the NdNiO_x slab obtained from a dynamical fit of the XRR⁶⁹ are $\ell_{PER} = 7.31$ nm, $\sigma_{PER} = 0.5$ nm before the reduction, and $\ell_{IL} = 6.20$ nm, $\sigma_{IL} = 1.9$ nm after. The thickness ratio of $\ell_{IL}/\ell_{PER} = 0.85$ matches the ratio of the c -axis lattice constants, 0.88—consistent with a full collapse of the structure without a substantial increase in the sample roughness. An RSM about the $\bar{1}03$ peaks of SrTiO₃ and NdNiO₂ shows that the coherence of the film is maintained through the reduction process. In a 00L scan of a 3 u.c. SrTiO₃ capped film (the supplementary material), all of the 001 through 004 reflections are visible in the IL film, and an out-of-plane lattice parameter of $c = 3.286$ Å is calculated from Nelson–Riley analysis,³⁰ in good agreement with previous measurements of chemically reduced films.^{40,70} A simulation of unreduced NdNiO₃/SrTiO₃ is fit to the XRD data in Fig. 5(f) to extract the setup parameters, which are then used to simulate the XRD for an NdNiO₂ film (changing only the structure from NdNiO₃ to NdNiO₂). Compared to a capped/reduced film, the observed pattern of Pendellösung fringes (and the Scherrer thickness) are correctly reproduced in the simulation, including the fringe spacing and the asymmetric intensity pattern.

C. Electrical transport measurements

The resistivity of a representative set of films reduced using the three-step procedure is shown in Fig. 6. Transport measurements of films with varying cap thickness show residual resistivities between 300 and 600 $\mu\Omega\text{-cm}$; this is lower than comparable undoped nickelate films on (001) SrTiO₃^{40,42,49} and comparable to underdoped films reported on (001) LSAT^{50,71} prepared by other methods. All samples show some degree of an upturn at low temperatures, between 20 and 35 K. Hall measurements, detailed in Fig. 6(b), show a flat temperature dependence of R_H between 75 and 300 K, consistent with prior measurements on undoped and underdoped NdNiO₂,^{38,40,41} accompanied by a downturn at low temperatures. The Hall coefficient, R_H , in the high temperature limit is around -0.01 cm³/C, which is intermediate to prior measurements of films on SrTiO₃, between -0.005 reported by Li *et al.*⁴⁰ and -0.035 as reported by Zeng *et al.*⁴¹ In contrast to prior measurements, a slight upturn in R_H is visible below 25 K. However, we note that the precise

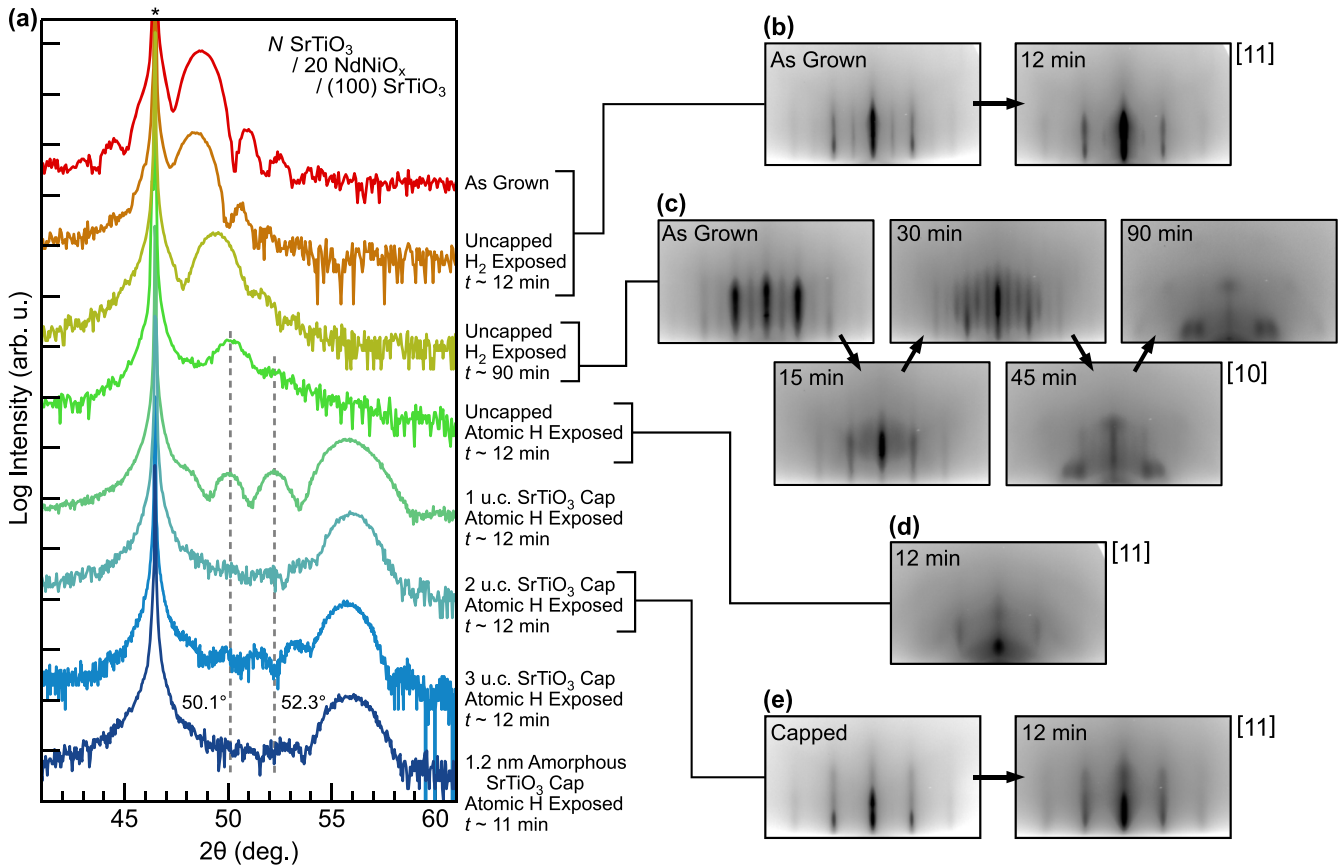


FIG. 7. Surface- and bulk-sensitive structural measurements of NdNiO_{3-x} films reduced using molecular and atomic hydrogen. (a) XRD of capped and uncapped nickelate samples exposed to molecular or atomic hydrogen. Dashed lines indicate the position of peaks likely derived from intermediately reduced phases, and (*) indicates reflections arising from the SrTiO_3 substrate; traces have been vertically offset for clarity. (b) RHEED images, taken with the electron beam along the $[110]_{pc}$ azimuth, of an uncapped perovskite film before and after a short exposure to molecular hydrogen. (c) RHEED images, taken with the electron beam along the $[100]_{pc}$ azimuth, of an uncapped film progressively exposed for longer periods, up to a total time of 1.5 h. (d) RHEED images, taken with the electron beam along the $[110]_{pc}$ azimuth, of an uncapped film exposed for a short duration to atomic hydrogen. (e) RHEED images, taken with the electron beam along the $[110]_{pc}$ azimuth, of a film capped with 2 u.c. of SrTiO_3 exposed to atomic hydrogen. All RHEED images use a logarithmic intensity scale. Samples were reduced under similar conditions with chamber pressures of $\sim 9 \times 10^{-5}$ Torr and sample temperatures range between 300 and 400 °C. Precise values of the times, temperatures, and fluxes used for each sample are tabulated in the supplementary material.

shape of $R_H(T)$ reported in the literature appears to vary considerably between different samples,^{40,41} A-site cations,⁴² and strain states.⁷¹

D. Effects of the capping layer

We conclude with a study of the effects of molecular and atomic hydrogen on film surfaces during reduction. Earlier reports have speculated on the role of the capping layer during reduction; our experiments reveal that exposure of the nickelate surface to a reducing atmosphere results in the formation of a polycrystalline scale layer on the sample surface. Furthermore, uncapped samples with this scale layer are *not* reduced under the same conditions, which are sufficient for the reduction of films capped with caps as thin as

1 u.c. of SrTiO_3 . In previous sections, we have described samples capped with 1–3 u.c. of SrTiO_3 and reduced with atomic hydrogen. Here, we describe what happens to films without a capping layer when they are exposed to H and H_2 . Figure 7(a) displays the XRD of a series of 20 u.c. thick films (capped and uncapped) following exposure to molecular or atomic hydrogen under similar conditions (chamber pressure and substrate temperature). Corresponding RHEED measurements for selected samples are included in Figs. 7(b)–7(e), and the specific details of each program are provided in the supplementary material. Exposure of an uncapped sample to molecular hydrogen for a short duration (<15 min) at a flux of 1.5×10^{15} $\text{H}_2/\text{cm}^2/\text{s}$ produces no apparent change in the XRD. However, the half-order streaks (associated with the rotation of the NiO_6 octahedra) are diminished, indicating a change in the surface oxygen stoichiometry. 15 min of additional exposure

produce 1/3rd order peaks, and with further reduction, the disappearance of film peaks and the formation of a secondary phase are observed. This degradation of the surface occurs at short timescales compared to the reduction of the entire film, as evidenced by the modest shift in the XRD. In addition, the total exposure of the film surface to H₂ gas in this experiment is low, limited to <10⁶ Langmuir (L) over 90 min, compared to hydride annealing experiments where the sample environment may contain up to 100 mTorr of hydrogen⁴¹ [liberated from CaH₂ or Ca(OH)₂^{44,72}] for several hours (~10⁹ L).

This surface degradation also affects oxygen removal during the atomic hydrogen reduction. When an uncapped film is reduced using the three-step process with nominally optimized conditions (12 min of total exposure), we observe a clear degradation of the RHEED pattern: the film peak intensity is reduced, background intensity increases, and faint polycrystalline rings appear. Surprisingly, this exposure does not produce an IL film; instead, a pair of intermediate phase peaks are observed at 2θ values of 50.1° and 52.3°. The addition of a capping layer greatly changes the process: using nearly identical time, temperature, and flux conditions, films with 1–3 layers of SrTiO₃ are reduced to the IL phase. In the 1 u.c. thick SrTiO₃ capped film, additional peaks are visible at positions not associated with Pendellösung fringes for this thickness film. These peaks, matching the positions of those in the uncapped film, suggest trace intermediate phases may remain, which are absent in the films capped with 2 or 3 u.c. of SrTiO₃. RHEED measurements show the capped films maintain an ordered surface, and AFM (the supplementary material) indicates a smooth, terraced surface is maintained, with a terrace-averaged roughness of only 1.2 Å. The substantial difference in oxygen removal between capped and uncapped films under the same reduction conditions highlights the cap's importance in facilitating the reduction process.

These extremely thin capping layers, approaching a single unit cell, likely do not substantially contribute to maintaining the structural stability across the entirety of the 20 u.c. film, yet they substantially influence the conditions required to reduce the film. This suggests that the cap plays a role beyond that of simple structural support and has a substantial impact on how easily oxygen is removed from the film. This distinction can be further explored by comparing the reduction of a sample capped with 3 u.c. of crystalline SrTiO₃ with one capped with 1.2 nm of amorphous SrTiO₃. We observe [cf. Fig. 7(a)] that samples capped with amorphous SrTiO₃ are well reduced using the three-step atomic hydrogen reduction procedure, even though the cap does not provide additional epitaxial support to the film. While films with either crystalline or amorphous SrTiO₃ caps are both reduced under similar conditions, there are some slight differences in the quality of the resulting IL films—discussed in the supplementary material—with amorphous SrTiO₃ capped films suffering from reduced crystallinity. The similarity between samples capped with crystalline and amorphous material, contrasted with the distinct behavior of uncapped samples, strongly suggests that during the atomic hydrogen reduction, the primary function of the cap is to prevent the formation of a nickelate scale layer at the sample surface rather than providing epitaxial stabilization of the IL phase. The contrast illustrated here may help to explain observed discrepancies between capped and uncapped

IL nickelate films in recent transport⁴³ and scattering⁷³ studies. We note that a recent study⁷⁴ has reported the successful synthesis of uncapped, Sr-doped (La,Sr)NiO₂ using atomic hydrogen reduction. This suggests that increasing the targeted valence of the Ni above 1+ by hole doping may sufficiently facilitate the reduction process, as observed in the reduction of bulk (Nd,Sr)NiO₂,⁶⁶ such that a capping layer may no longer be necessary to fully reduce the doped materials.

IV. CONCLUSIONS

Here, we have described a novel, flexible synthesis method for IL nickelate films—one that requires only gas phase reactants and is easily integrable with thin film growth techniques and surface sensitive probes. Characterization of the resulting films shows this method reproducibly yields IL films with high crystallinity, low resistivity, and flat surfaces. Utilizing the *in situ* nature of this procedure, we have investigated the effects of the reduction on the film surface to elucidate the impact of capping layers on the reaction. We find that the addition of an ultrathin cap, down to 0.4–1.2 nm, drastically improves the reduction process and inhibits the formation of a polycrystalline scale layer on the sample surface. In addition, we have demonstrated the growth of high quality films of NdNiO₃ by MBE and illustrated that the structural and electrical characteristics of the highly strained perovskite are unstable over a timescale of hours to days. Diffraction and real-space probes indicate that the sample strain is partially relieved by the rapid formation of cracks soon after growth. These measurements indicate that care must be taken when investigating the details of the MIT in highly strained nickelates, as well as unveiling a potentially uncontrolled variable in nickelate reduction experiments. Topotactically reduced oxides have proven to be a rich, expanding field for the investigation of novel ground states in quantum materials;^{1,23,35,59,75–82} we put forth atomic hydrogen reduction as a highly tunable process for synthesizing reduced oxides of high quality. The vacuum compatibility of this technique both expands the range of experiments that may be performed on reduced films and enables *in situ* and *operando* studies of the reduction process itself.

V. METHODS

A. Sample growth, reduction, and characterization

Thin films of NdNiO₃ were grown on (001)-oriented SrTiO₃ substrates using reactive-oxide molecular-beam epitaxy (MBE) in a Veeco GEN10 system from elemental beams of Nd (Alfa/AESAR, 99.9%) and Ni (Alfa/AESAR, 99.995%) with typical fluxes of 0.8–1.2 × 10¹³ at./cm²/s. Substrates were etched to prepare a TiO₂ terminated surface⁸³ and annealed prior to growth at 650 °C until a clear RHEED pattern was observed. Growths were performed at substrate temperatures between 480 and 500 °C, measured by optical pyrometry at a wavelength of 1550 nm, in background pressures between 2 and 7 × 10⁻⁶ Torr of ~80% distilled ozone. Following growth, samples were cooled to <100 °C at a pressure of >1 × 10⁻⁶ Torr of ozone to discourage the formation of oxygen vacancies.

Reduction experiments were performed in an ultra-high vacuum chamber with a base pressure better than 1 × 10⁻¹⁰ Torr, connected to the MBE system by a vacuum manifold with a pres-

sure better than 1×10^{-9} Torr. For the reductions discussed in this work, the same hydrogen flow rate through the cracker, 0.72 sccm, was used for all samples, and the atomic hydrogen flux was tuned by changing the temperature of the tungsten capillary (monitored using an integrated thermocouple). This procedure results in a background chamber pressure of $9\text{--}10 \times 10^{-6}$ Torr during the reaction. As a control, an SrTiO_3 substrate was ozone annealed to prepare a clean surface and then subjected to the same reduction conditions as the nickelate samples. No changes were observable in the RHEED pattern of the substrate, and no conductivity was detectable following its removal from vacuum.

Structural quality and phase purity were determined using $\text{Cu K}\alpha_1$ x-ray diffraction measurements performed on a PANalytical Empyrean x-ray diffractometer. Morphology was assessed using an Asylum Research Cypher environmental atomic force microscope. Electrical transport measurements were performed using both a custom built LHe-cooled four-point probe measurement station and a Quantum Design physical property measurement system utilizing either built-in electronics or a Keithley 6221 current source and 2182A voltmeter in a delta mode configuration. Geometric factors in the resistivity were accounted for using the methods in Ref. 84. Hall measurements were performed either over the entire $10 \times 10 \text{ mm}^2$ sample in a square four-point Van der Pauw configuration or using a six-wire Hall bar geometry on a diced $5 \times 10 \text{ mm}$ piece.

B. Scanning transmission electron microscopy

Cross-sectional specimens were prepared using the standard focused ion beam (FIB) lift-out process on a Thermo Fisher Scientific G4 UX FIB. HAADF-STEM images were acquired on an aberration-corrected FEI Titan Themis operating at 300 kV with a probe-forming semi-angle of 21.4 mrad and inner (outer) collection angles of 68 (340) mrad. To avoid possible image distortions from sample drift or other mechanical instabilities, all images presented here are produced by summing a stack of 50 high-frame-rate images aligned by rigid registration.⁸⁵ A small-angle shear transformation was applied to all images to correct for subtle non-orthogonality in the STEM scan. Lattice relaxation in the film was mapped with strain analysis based on a phase lock-in approach.³⁴

SUPPLEMENTARY MATERIAL

See the supplementary material for additional details about the stoichiometric calibration process, further data on the effects of non-stoichiometry and strain relaxation on transport measurements, and additional details about the effects of the reduction process on capped and uncapped films.

ACKNOWLEDGMENTS

This work was primarily supported by the National Science Foundation through Grant No. DMR-2104427 and the Platform for the Accelerated Realization, Analysis, and Discovery of Interface Materials (PARADIM) under Cooperative Agreement No. DMR-2039380. Additional support was provided by the Air Force Office of Scientific Research (Grant No. FA9550-21-1-0168) and the Gordon and Betty Moore Foundation's EPiQS Initiative through Grant

Nos. GBMF3850 and GBMF9073. The authors acknowledge the use of facilities and instrumentation supported by NSF through the Cornell University Materials Research Science and Engineering Center DMR-1719875. The FEI Titan Themis 300 was acquired through Grant No. NSF-MRI-1429155, with additional support from Cornell University, the Weill Institute, and the Kavli Institute at Cornell. The Thermo Fisher Helios G4 UX FIB was acquired with support from NSF Grant No. DMR-1539918. Substrate preparation was performed, in part, at the Cornell NanoScale Facility, a member of the National Nanotechnology Coordinated Infrastructure (NNCI), which is supported by the National Science Foundation (Grant No. NNCI-2025233). The authors would like to thank Sean Palmer and Steven Button for their assistance in substrate preparation, as well as Hari Nair and Jiaxin Sun for their thoughtful discussions and insightful comments.

AUTHOR DECLARATIONS

Conflict of Interest

The authors have no conflicts to disclose.

Author Contributions

Samples were synthesized, reduced, and characterized by C.T.P., V.A., Y.W., and M.R. under the supervision of D.G.S. and K.M.S. Electron microscopy was performed by B.H.G. under the supervision of L.F.K. The manuscript was prepared by C.T.P. and K.M.S. with input from all authors.

C. T. Parzyck: Conceptualization (equal); Data curation (equal); Formal analysis (equal); Investigation (equal); Methodology (equal); Visualization (equal); Writing – original draft (equal); Writing – review & editing (equal). **V. Anil:** Formal analysis (equal); Investigation (equal); Writing – review & editing (equal). **Y. Wu:** Formal analysis (equal); Investigation (equal); Writing – review & editing (equal). **B. H. Goodge:** Formal analysis (equal); Investigation (equal); Writing – review & editing (equal). **M. Roddy:** Formal analysis (equal); Investigation (equal); Writing – review & editing (equal). **L. F. Kourkoutis:** Funding acquisition (equal); Project administration (equal); Resources (equal); Supervision (equal). **D. G. Schlom:** Funding acquisition (equal); Project administration (equal); Resources (equal); Supervision (equal). **K. M. Shen:** Funding acquisition (equal); Project administration (equal); Resources (equal); Supervision (equal); Writing – original draft (equal); Writing – review & editing (equal).

DATA AVAILABILITY

The data that support the findings of this study are available within the paper and supplementary material. Data acquired and analyzed during the course of the study are available at DOI [10.34863/44w9-wc96](https://doi.org/10.34863/44w9-wc96).

REFERENCES

- ¹D. Li, K. Lee, B. Y. Wang, M. Osada, S. Crossley, H. R. Lee, Y. Cui, Y. Hikita, and H. Y. Hwang, "Superconductivity in an infinite-layer nickelate," *Nature* **572**, 624–627 (2019).

- ²M. Osada, B. Y. Wang, B. H. Goodge, K. Lee, H. Yoon, K. Sakuma, D. Li, M. Miura, L. F. Kourkoutis, and H. Y. Hwang, "A superconducting praseodymium nickelate with infinite layer structure," *Nano Lett.* **20**, 5735–5740 (2020).
- ³M. Osada, B. Y. Wang, B. H. Goodge, S. P. Harvey, K. Lee, D. Li, L. F. Kourkoutis, and H. Y. Hwang, "Nickelate superconductivity without rare-earth magnetism: (La,Sr)NiO₂," *Adv. Mater.* **33**, 2104083 (2021).
- ⁴S. Zeng, C. Li, L. E. Chow, Y. Cao, Z. Zhang, C. S. Tang, X. Yin, Z. S. Lim, J. Hu, P. Yang, and A. Ariando, "Superconductivity in infinite-layer nickelate La_{1-x}Ca_xNiO₂ thin films," *Sci. Adv.* **8**, eabl9927 (2022).
- ⁵J. Zhang, H. Zheng, Y. Ren, and J. F. Mitchell, "High-pressure floating-zone growth of perovskite nickelate LaNiO₃ single crystals," *Cryst. Growth Des.* **17**, 2730–2735 (2017).
- ⁶H. Zheng, J. Zhang, B. Wang, D. Phelan, M. J. Krogstad, Y. Ren, W. A. Phelan, O. Chmaissem, B. Poudel, and J. F. Mitchell, "High pO₂ floating zone crystal growth of the perovskite nickelate PrNiO₃," *Crystals* **9**, 324 (2019).
- ⁷P. Pupal, Y.-M. Wu, K. Fürsich, H. Lee, M. Pakdaman, J. A. N. Bruin, J. Nuss, Y. E. Suyolcu, P. A. van Aken, B. Keimer, M. Isobe, and M. Hepting, "Topotactic transformation of single crystals: From perovskite to infinite-layer nickelates," *Sci. Adv.* **7**, eabl8091 (2021).
- ⁸P. Pupal, V. Pomjakushin, R. A. Ortiz, S. Hammoud, M. Isobe, B. Keimer, and M. Hepting, "Investigation of hydrogen incorporations in bulk infinite-layer nickelates," *Front. Phys.* **10**, 1–6 (2022).
- ⁹M. Huo, Z. Liu, H. Sun, L. Li, H. Lui, C. Huang, F. Liang, B. Shen, and M. Wang, "Synthesis and properties of La_{1-x}Sr_xNiO₃ and La_{1-x}Sr_xNiO₂," *Chin. Phys. B* **31**, 107401 (2022).
- ¹⁰P. Pupal, B. Wehinger, J. Nuss, K. Küster, U. Starke, G. Garbarino, B. Keimer, M. Isobe, and M. Hepting, "Synthesis and physical properties of LaNiO₂ crystals," *Phys. Rev. Mater.* **7**, 014804 (2023).
- ¹¹Y.-M. Wu, P. Pupal, H. Lee, J. Nuss, M. Isobe, B. Keimer, M. Hepting, Y. E. Suyolcu, and P. A. van Aken, "Topotactically induced oxygen vacancy order in nickelate single crystals," *Phys. Rev. Mater.* **7**, 053609 (2023).
- ¹²C. Domínguez, A. B. Georgescu, B. Mundet, Y. Zhang, J. Fowlie, A. Mercy, A. Waelchli, S. Catalano, D. T. Alexander, P. Ghosez, A. Georges, A. J. Millis, M. Gibert, and J. M. Triscone, "Length scales of interfacial coupling between metal and insulator phases in oxides," *Nat. Mater.* **19**, 1182–1187 (2020).
- ¹³Q. Song, S. Doyle, G. A. Pan, I. El Baggari, D. Ferenc Segedin, D. Córdoba Carrizales, J. Nordlander, C. Tzschaschel, J. R. Ehrets, Z. Hasan, H. El-Sherif, J. Krishna, C. Hanson, H. LaBollita, A. Bostwick, C. Jozwiak, E. Rotenberg, S.-Y. Xu, A. Lanzara, A. T. N'Diaye, C. A. Heikes, Y. Liu, H. Paik, C. M. Brooks, B. Pamuk, J. T. Heron, P. Shafer, W. D. Ratcliff, A. S. Botana, L. Moreschini, and J. A. Mundy, "Antiferromagnetic metal phase in an electron-doped rare-earth nickelate," *Nat. Phys.* **19**, 522–528 (2023).
- ¹⁴C. Domínguez, J. Fowlie, A. B. Georgescu, B. Mundet, N. Jaouen, M. Viret, A. Suter, A. J. Millis, Z. Salman, T. Prokscha, M. Gibert, and J.-M. Triscone, "Coupling of magnetic phases at nickelate interfaces," *Phys. Rev. Mater.* **7**, 065002 (2023).
- ¹⁵E. Breckenfeld, Z. Chen, A. R. Damodaran, and L. W. Martin, "Effects of nonequilibrium growth, nonstoichiometry, and film orientation on the metal-insulator transition in NdNiO₃ thin films," *ACS Appl. Mater. Interfaces* **6**, 22436–22444 (2014).
- ¹⁶D. Preziosi, A. Sander, A. Barthélémy, and M. Bibes, "Reproducibility and off-stoichiometry issues in nickelate thin films grown by pulsed laser deposition," *AIP Adv.* **7**, 015210 (2017).
- ¹⁷T. Yamanaka, A. N. Hattori, L. N. Pamasí, S. Takemoto, K. Hattori, H. Daimon, K. Sato, and H. Tanaka, "Effects of off-stoichiometry in the epitaxial NdNiO₃ film on the suppression of its metal-insulator-transition properties," *ACS Appl. Electron. Mater.* **1**, 2678–2683 (2019).
- ¹⁸Y. Li, W. Sun, J. Yang, X. Cai, W. Guo, Z. Gu, Y. Zhu, and Y. Nie, "Impact of cation stoichiometry on the crystalline structure and superconductivity in nickelates," *Front. Phys.* **9**, 1–12 (2021).
- ¹⁹S. Heo, C. Oh, J. Son, and H. M. Jang, "Influence of tensile-strain-induced oxygen deficiency on metal-insulator transitions in NdNiO_{3-δ} epitaxial thin films," *Sci. Rep.* **7**, 4681 (2017).
- ²⁰A. J. Hauser, E. Mikheev, N. E. Moreno, J. Hwang, J. Y. Zhang, and S. Stemmer, "Correlation between stoichiometry, strain, and metal-insulator transitions of NdNiO₃ films," *Appl. Phys. Lett.* **106**, 092104 (2015).
- ²¹D. Ferenc Segedin, B. H. Goodge, G. A. Pan, Q. Song, H. LaBollita, M.-C. Jung, H. El-Sherif, S. Doyle, A. Turkiewicz, N. K. Taylor, J. A. Mason, A. T. N'Diaye, H. Paik, I. El Baggari, A. S. Botana, L. F. Kourkoutis, C. M. Brooks, and J. A. Mundy, "Limits to the strain engineering of layered square-planar nickelate thin films," *Nat. Commun.* **14**, 1468 (2023).
- ²²K. Lee, B. H. Goodge, D. Li, M. Osada, B. Y. Wang, Y. Cui, L. F. Kourkoutis, and H. Y. Hwang, "Aspects of the synthesis of thin film superconducting infinite-layer nickelates," *APL Mater.* **8**, 041107 (2020).
- ²³M. A. Hayward, M. A. Green, M. J. Rosseinsky, and J. Sloan, "Sodium hydride as a powerful reducing agent for topotactic oxide deintercalation: Synthesis and characterization of the nickel(I) oxide LaNiO₂," *J. Am. Chem. Soc.* **121**, 8843–8854 (1999).
- ²⁴M. Hayward and M. Rosseinsky, "Synthesis of the infinite layer Ni(I) phase NdNiO_{2+x} by low temperature reduction of NdNiO₃ with sodium hydride," *Solid State Sci.* **5**, 839–850 (2003).
- ²⁵K. G. Tschersich and V. von Bonin, "Formation of an atomic hydrogen beam by a hot capillary," *J. Appl. Phys.* **84**, 4065–4070 (1998).
- ²⁶K. G. Tschersich, J. P. Fleischhauer, and H. Schuler, "Design and characterization of a thermal hydrogen atom source," *J. Appl. Phys.* **104**, 034908 (2008).
- ²⁷P.-H. Xiang, N. Zhong, C.-G. Duan, X. D. Tang, Z. G. Hu, P. X. Yang, Z. Q. Zhu, and J. H. Chu, "Strain controlled metal-insulator transition in epitaxial NdNiO₃ thin films," *J. Appl. Phys.* **114**, 243713 (2013).
- ²⁸P. D. C. King, H. I. Wei, Y. F. Nie, M. Uchida, C. Adamo, S. Zhu, X. He, I. Božović, D. G. Schlom, and K. M. Shen, "Atomic-scale control of competing electronic phases in ultrathin LaNiO₃," *Nat. Nanotechnol.* **9**, 443–447 (2014).
- ²⁹J. Sun, C. T. Parzyck, J. H. Lee, C. M. Brooks, L. F. Kourkoutis, X. Ke, R. Misra, J. Schubert, F. V. Hensling, M. R. Barone, Z. Wang, M. E. Holtz, N. J. Schreiber, Q. Song, H. Paik, T. Heeg, D. A. Muller, K. M. Shen, and D. G. Schlom, "Canonical approach to cation flux calibration in oxide molecular-beam epitaxy," *Phys. Rev. Mater.* **6**, 033802 (2022).
- ³⁰J. B. Nelson and D. P. Riley, "An experimental investigation of extrapolation methods in the derivation of accurate unit-cell dimensions of crystals," *Proc. Phys. Soc.* **57**, 160–177 (1945).
- ³¹G. A. Pan, Q. Song, D. Ferenc Segedin, M. C. Jung, H. El-Sherif, E. E. Fleck, B. H. Goodge, S. Doyle, D. Córdoba Carrizales, A. T. N'Diaye, P. Shafer, H. Paik, L. F. Kourkoutis, I. El Baggari, A. S. Botana, C. M. Brooks, and J. A. Mundy, "Synthesis and electronic properties of Nd_{n+1}Ni_nO_{3n+1} Ruddlesden-Popper nickelate thin films," *Phys. Rev. Mater.* **6**, 055003 (2022).
- ³²Y. M. Klein, M. Kozłowski, A. Linden, P. Lacorre, M. Medarde, and D. J. Gawryluk, "RENiO₃ single crystals (RE = Nd, Sm, Gd, Dy, Y, Ho, Er, Lu) grown from molten salts under 2000 bar of oxygen gas pressure," *Cryst. Growth Des.* **21**, 4230–4241 (2021).
- ³³M. D. Biegalski, D. D. Fong, J. A. Eastman, P. H. Fuoss, S. K. Streiffer, T. Heeg, J. Schubert, W. Tian, C. T. Nelson, X. Q. Pan, M. E. Hawley, M. Bernhagen, P. Reiche, R. Uecker, S. Trolier-McKinstry, and D. G. Schlom, "Critical thickness of high structural quality SrTiO₃ films grown on orthorhombic (101) DyScO₃," *J. Appl. Phys.* **104**, 114109 (2008).
- ³⁴B. H. Goodge, I. El Baggari, S. S. Hong, Z. Wang, D. G. Schlom, H. Y. Hwang, and L. F. Kourkoutis, "Disentangling coexisting structural order through phase lock-in analysis of atomic-resolution STEM data," *Microsc. Microanal.* **28**, 404–411 (2022).
- ³⁵M. Crespin, P. Levitz, and L. Gataineau, "Reduced forms of LaNiO₃ perovskite," *J. Chem. Soc., Faraday Trans. II* **79**, 1181 (1983).
- ³⁶M. Crespin, O. Isnard, F. Dubois, J. Choisnet, and P. Odier, "LaNiO₂: Synthesis and structural characterization," *J. Solid State Chem.* **178**, 1326–1334 (2005).
- ³⁷M. Kawai, S. Inoue, M. Mizumaki, N. Kawamura, N. Ichikawa, and Y. Shimakawa, "Reversible changes of epitaxial thin films from perovskite LaNiO₃ to infinite-layer structure LaNiO₂," *Appl. Phys. Lett.* **94**, 082102 (2009).
- ³⁸A. Ikeda, Y. Krockenberger, H. Irie, M. Naito, and H. Yamamoto, "Direct observation of infinite NiO₂ planes in LaNiO₂ films," *Appl. Phys. Express* **9**, 061101 (2016).
- ³⁹T. Onozuka, A. Chikamatsu, T. Katayama, T. Fukumura, and T. Hasegawa, "Formation of defect-fluorite structured NdNiO₃H₂ epitaxial thin films via a soft chemical route from NdNiO₃ precursors," *Dalton Trans.* **45**, 12114–12118 (2016).

- ⁴⁰D. Li, B. Y. Wang, K. Lee, S. P. Harvey, M. Osada, B. H. Goodge, L. F. Kourkoutis, and H. Y. Hwang, "Superconducting dome in Nd_{1-x}Sr_xNiO₂ infinite layer films," *Phys. Rev. Lett.* **125**, 027001 (2020).
- ⁴¹S. Zeng, C. S. Tang, X. Yin, C. Li, M. Li, Z. Huang, J. Hu, W. Liu, G. J. Omar, H. Jani, Z. S. Lim, K. Han, D. Wan, P. Yang, S. J. Pennycook, A. T. S. Wee, and A. Ariando, "Phase diagram and superconducting dome of infinite-layer Nd_{1-x}Sr_xNiO₂ thin films," *Phys. Rev. Lett.* **125**, 147003 (2020).
- ⁴²M. Osada, B. Y. Wang, K. Lee, D. Li, and H. Y. Hwang, "Phase diagram of infinite layer praseodymium nickelate Pr_{1-x}Sr_xNiO₂ thin films," *Phys. Rev. Mater.* **4**, 121801 (2020).
- ⁴³G. Krieger, A. Raji, L. Schlur, G. Versini, C. Bouillet, M. Lenertz, J. Robert, A. Gloter, N. Viart, and D. Preziosi, "Synthesis of infinite-layer nickelates and influence of the capping-layer on magnetotransport," *J. Phys. D: Appl. Phys.* **56**, 024003 (2023).
- ⁴⁴A. Ikeda, T. Manabe, and M. Naito, "Comparison of reduction agents in the synthesis of infinite-layer LaNiO₂ films," *Physica C* **506**, 83–86 (2014).
- ⁴⁵Q. Gao, Y. Zhao, X.-J. Zhou, and Z. Zhu, "Preparation of superconducting thin films of infinite-layer nickelate Nd_{0.8}Sr_{0.2}NiO₂," *Chin. Phys. Lett.* **38**, 077401 (2021).
- ⁴⁶Q. Gu, Y. Li, S. Wan, H. Li, W. Guo, H. Yang, Q. Li, X. Zhu, X. Pan, Y. Nie, and H. H. Wen, "Single particle tunneling spectrum of superconducting Nd_{1-x}Sr_xNiO₂ thin films," *Nat. Commun.* **11**, 6027 (2020).
- ⁴⁷Z. Chen, M. Osada, D. Li, E. M. Been, S. D. Chen, M. Hashimoto, D. Lu, S. K. Mo, K. Lee, B. Y. Wang, F. Rodolakis, J. L. McChesney, C. Jia, B. Moritz, T. P. Devereaux, H. Y. Hwang, and Z. X. Shen, "Electronic structure of superconducting nickelates probed by resonant photoemission spectroscopy," *Matter* **5**, 1806–1815 (2022).
- ⁴⁸R.-F. Wang, Y.-L. Xiong, H. Yan, X. Hu, M. Osada, D. Li, H. Y. Hwang, C.-L. Song, X.-C. Ma, and Q.-K. Xue, "Observation of Coulomb blockade and Coulomb staircases in superconducting Pr_{0.8}Sr_{0.2}NiO₂ films," *Phys. Rev. B* **107**, 115411 (2023).
- ⁴⁹W. Wei, K. Shin, H. Hong, Y. Shin, A. S. Thind, Y. Yang, R. F. Klie, F. J. Walker, and C. H. Ahn, "Solid state reduction of nickelate thin films," *Phys. Rev. Mater.* **7**, 013802 (2023).
- ⁵⁰W. Wei, D. Vu, Z. Zhang, F. J. Walker, and C. H. Ahn, "Superconducting Nd_{1-x}Eu_xNiO₂ thin films using in situ synthesis," *Sci. Adv.* **9**, eadh3327 (2023).
- ⁵¹A. A. Bergh, "Atomic hydrogen as a reducing agent," *Bell Syst. Tech. J.* **44**, 261–271 (1965).
- ⁵²S. M. Gates, R. R. Kunz, and C. Greenlief, "Silicon hydride etch products from the reaction of atomic hydrogen with Si(100)," *Surf. Sci.* **207**, 364–384 (1989).
- ⁵³G. Bell, N. Kaijaks, R. Dixon, and C. McConville, "Atomic hydrogen cleaning of polar III–V semiconductor surfaces," *Surf. Sci.* **401**, 125–137 (1998).
- ⁵⁴I. Nishiyama, H. Oizumi, K. Motai, A. Izumi, T. Ueno, H. Akiyama, and A. Namiki, "Reduction of oxide layer on Ru surface by atomic-hydrogen treatment," *J. Vac. Sci. Technol. B* **23**, 3129–3131 (2005).
- ⁵⁵W. Huang, W. Ranke, and R. Schlögl, "Reduction of an α -Fe₂O₃(0001) film using atomic hydrogen," *J. Phys. Chem. C* **111**, 2198–2204 (2007).
- ⁵⁶J. Knudsen, L. R. Merte, L. C. Grabow, F. M. Eichhorn, S. Porsgaard, H. Zeuthen, R. T. Vang, E. Lægsgaard, M. Mavrikakis, and F. Besenbacher, "Reduction of FeO/Pt(111) thin films by exposure to atomic hydrogen," *Surf. Sci.* **604**, 11–20 (2010).
- ⁵⁷S. M. F. Shahed, T. Hasegawa, Y. Sainoo, Y. Watanabe, N. Isomura, A. Beniya, H. Hirata, and T. Komeda, "STM and XPS study of CeO₂(111) reduction by atomic hydrogen," *Surf. Sci.* **628**, 30–35 (2014).
- ⁵⁸K. Takahashi, D. Matthey, D. Jaccard, and J.-M. Triscone, "Transport properties of reduced SrTiO₃ single crystal 'thin films,'" *Ann. Phys.* **13**, 68–69 (2004).
- ⁵⁹Z. Meng, H. Yan, P. Qin, X. Zhou, X. Wang, H. Chen, L. Liu, and Z. Liu, "Topotactic transition: A promising opportunity for creating new oxides," *Adv. Funct. Mater.* **33**, 1–48 (2023).
- ⁶⁰W. Zheng and A. Gallagher, "Hydrogen dissociation on high-temperature tungsten," *Surf. Sci.* **600**, 2207–2213 (2006).
- ⁶¹J. M. González-Calbet, M. J. Sayagués, and M. Vallet-Regí, "An electron diffraction study of new phases in the LaNiO_{3-x} system," *Solid State Ionics* **32–33**, 721–726 (1989).
- ⁶²T. Moriga, O. Usaka, I. Nakabayashi, Y. Hirashima, T. Kohno, S. Kikkawa, and F. Kanamaru, "Reduction of the perovskite-type LnNiO₃ (Ln = Pr, Nd) to Ln₃Ni₃O₇ with monovalent nickel ions," *Solid State Ionics* **74**, 211–217 (1994).
- ⁶³M. Sayagués, M. Vallet-Regí, A. Caneiro, and J. González-Calbet, "Microstructural characterization of the LaNiO_{3-y} system," *J. Solid State Chem.* **110**, 295–304 (1994).
- ⁶⁴J. A. Alonso and M. J. Martínez-Lope, "Preparation and crystal structure of the deficient perovskite LaNiO_{2.5}, solved from neutron powder diffraction data," *J. Chem. Soc., Dalton Trans.* **1995**, 2819–2824 (1995).
- ⁶⁵T. Moriga, M. Hayashi, T. Sakamoto, M. Orihara, and I. Nakabayashi, "Reduction processes of rare-earth nickelate perovskites LnNiO₃ (Ln = La, Pr, Nd)," *Solid State Ionics* **154–155**, 251–255 (2002).
- ⁶⁶B.-X. Wang, H. Zheng, E. Krivyakina, O. Chmaissem, P. P. Lopes, J. W. Lynn, L. C. Gallington, Y. Ren, S. Rosenkranz, J. F. Mitchell, and D. Phelan, "Synthesis and characterization of bulk Nd_{1-x}Sr_xNiO₂ and Nd_{1-x}Sr_xNiO₃," *Phys. Rev. Mater.* **4**, 084409 (2020).
- ⁶⁷A. Raji, G. Krieger, N. Viart, D. Preziosi, J.-P. Rueff, and A. Gloter, "Charge distribution across capped and uncapped infinite-layer neodymium nickelate thin films," *Small* **19**, 2304872 (2023).
- ⁶⁸C. T. Parzyck, N. K. Gupta, Y. Wu, V. Anil, L. Bhatt, M. Bouliane, R. Gong, B. Z. Gregory, A. Luo, R. Sutarto, F. He, Y.-D. Chuang, T. Zhou, G. Herranz, L. F. Kourkoutis, A. Singer, D. G. Schlom, D. G. Hawthorn, and K. M. Shen, "Absence of 3a₀ charge density wave order in the infinite-layer nickelate NdNiO₂," *Nat. Mater.* (published online, 2024).
- ⁶⁹D. Krieger, E. Wintersberger, and J. Stangl, "xrayutilities: a versatile tool for reciprocal space conversion of scattering data recorded with linear and area detectors," *J. Appl. Crystallogr.* **46**, 1162–1170 (2013).
- ⁷⁰B. H. Goodge, B. Geisler, K. Lee, M. Osada, B. Y. Wang, D. Li, H. Y. Hwang, R. Pentcheva, and L. F. Kourkoutis, "Resolving the polar interface of infinite-layer nickelate thin films," *Nat. Mater.* **22**, 466–473 (2023); [arXiv:2201.03613](https://arxiv.org/abs/2201.03613).
- ⁷¹K. Lee, B. Y. Wang, M. Osada, B. H. Goodge, T. C. Wang, Y. Lee, S. Harvey, W. J. Kim, Y. Yu, C. Murthy, S. Raghu, L. F. Kourkoutis, and H. Y. Hwang, "Linear-in-temperature resistivity for optimally superconducting (Nd,Sr)NiO₂," *Nature* **619**, 288–292 (2023).
- ⁷²Y. Kobayashi, Z. Li, K. Hirai, C. Tassel, F. Loyer, N. Ichikawa, N. Abe, T. Yamamoto, Y. Shimakawa, K. Yoshimura, M. Takano, O. J. Hernandez, and H. Kageyama, "Gas phase contributions to topochemical hydride reduction reactions," *J. Solid State Chem.* **207**, 190–193 (2013).
- ⁷³G. Krieger, L. Martinelli, S. Zeng, L. E. Chow, K. Kummer, R. Arpaia, M. Moretti Sala, N. B. Brookes, A. Ariando, N. Viart, M. Salluzzo, G. Ghiringhelli, and D. Preziosi, "Charge and spin order dichotomy in NdNiO₂ driven by the capping layer," *Phys. Rev. Lett.* **129**, 027002 (2022).
- ⁷⁴W. Sun, Z. Wang, B. Hao, S. Yan, H. Sun, Z. Gu, Y. Deng, and Y. Nie, "In situ preparation of superconducting infinite-layer nickelate thin films with atomically flat surface," [arXiv:2401.15979](https://arxiv.org/abs/2401.15979) [cond-mat.supr-con] (2024).
- ⁷⁵G. A. Pan, D. Ferenc Segedin, H. LaBollita, Q. Song, E. M. Nica, B. H. Goodge, A. T. Pierce, S. Doyle, S. Novakov, D. Córdoba Carrizales, A. T. N'Diaye, P. Shafer, H. Paik, J. T. Heron, J. A. Mason, A. Yacoby, L. F. Kourkoutis, O. Erten, C. M. Brooks, A. S. Botana, and J. A. Mundy, "Superconductivity in a quintuple-layer square-planar nickelate," *Nat. Mater.* **21**, 160–164 (2022).
- ⁷⁶W. J. Kim, M. A. Smeaton, C. Jia, B. H. Goodge, B.-G. Cho, K. Lee, M. Osada, D. Jost, A. V. Ievlev, B. Moritz, L. F. Kourkoutis, T. P. Devereaux, and H. Y. Hwang, "Geometric frustration of Jahn–Teller order in the infinite-layer lattice," *Nature* **615**, 237–243 (2023).
- ⁷⁷Y. Tsujimoto, C. Tassel, N. Hayashi, T. Watanabe, H. Kageyama, K. Yoshimura, M. Takano, M. Ceretti, C. Ritter, and W. Paulus, "Infinite-layer iron oxide with a square-planar coordination," *Nature* **450**, 1062–1065 (2007).
- ⁷⁸S. Inoue, M. Kawai, Y. Shimakawa, M. Mizumaki, N. Kawamura, T. Watanabe, Y. Tsujimoto, H. Kageyama, and K. Yoshimura, "Single-crystal epitaxial thin films of SrFeO₂ with FeO₂ 'infinite layers,'" *Appl. Phys. Lett.* **92**, 161911 (2008).
- ⁷⁹J. Hadermann, A. M. Abakumov, J. J. Adkin, and M. A. Hayward, "Topotactic reduction as a route to new close-packed anion deficient perovskites:

Structure and magnetism of 4H-BaMnO_{2+x},” *J. Am. Chem. Soc.* **131**, 10598–10604 (2009).

⁸⁰K. Matsumoto, M. Haruta, M. Kawai, A. Sakaiguchi, N. Ichikawa, H. Kurata, and Y. Shimakawa, “Artificial superlattice thin film of infinite-layer structure [CaFeO₂]/[SrFeO₂],” *Appl. Phys. Express* **3**, 105601 (2010).

⁸¹E. J. Moon, Y. Xie, E. D. Laird, D. J. Keavney, C. Y. Li, and S. J. May, “Fluorination of epitaxial oxides: Synthesis of perovskite oxyfluoride thin films,” *J. Am. Chem. Soc.* **136**, 2224–2227 (2014).

⁸²T. Mairoser, J. A. Mundy, A. Melville, D. Hodash, P. Cueva, R. Held, A. Glavic, J. Schubert, D. A. Muller, D. G. Schlom, and A. Schmehl, “High-quality EuO thin films the easy way via topotactic transformation,” *Nat. Commun.* **6**, 7716 (2015).

⁸³G. Koster, B. L. Kropman, G. J. H. M. Rijnders, D. H. A. Blank, and H. Rogalla, “Quasi-ideal strontium titanate crystal surfaces through formation of strontium hydroxide,” *Appl. Phys. Lett.* **73**, 2920–2922 (1998).

⁸⁴I. Miccoli, F. Edler, H. Pfnür, and C. Tegenkamp, “The 100th anniversary of the four-point probe technique: The role of probe geometries in isotropic and anisotropic systems,” *J. Phys.: Condens. Matter* **27**, 223201 (2015).

⁸⁵B. H. Savitzky, I. El Baggari, C. B. Clement, E. Waite, B. H. Goodge, D. J. Baek, J. P. Shekelton, C. Pasco, H. Nair, N. J. Schreiber, J. Hoffman, A. S. Admasu, J. Kim, S.-W. Cheong, A. Bhattacharya, D. G. Schlom, T. M. McQueen, R. Hovden, and L. F. Kourkoutis, “Image registration of low signal-to-noise cryo-STEM data,” *Ultramicroscopy* **191**, 56–65 (2018).

Supplemental Materials for: Synthesis of thin film infinite-layer nickelates by atomic hydrogen reduction: clarifying the role of the capping layer

C. T. Parzyck,¹ V. Anil,¹ Y. Wu,¹ B. H. Goodge,^{2,3} M. Roddy,¹
L. F. Kourkoutis,^{2,3} D. G. Schlom,^{3,4,5} and K. M. Shen^{1,3,6}

¹*Laboratory of Atomic and Solid State Physics, Department of Physics, Cornell University, Ithaca, NY 14853, USA*

²*School of Applied and Engineering Physics, Cornell University, Ithaca, NY 14853, USA*

³*Kavli Institute at Cornell for Nanoscale Science, Cornell University, Ithaca, NY 14853, USA*

⁴*Department of Materials Science and Engineering, Cornell University, Ithaca, NY 14853, USA*

⁵*Leibniz-Institut für Kristallzüchtung, Max-Born-Straße 2, 12489 Berlin, Germany*

⁶*Institut de Ciència de Materials de Barcelona (ICMAB-CSIC), Campus UAB Bellaterra 08193, Spain*

(Dated: February 25, 2024)

CONTENTS

I. Perovskite Nickelates	2
A. RHEED Oscillation Calibration	2
B. XRD and XRR Calibration	3
C. Effects of Non-Stoichiometry on Transport	4
D. Additional Aging Effect Data	4
II. Infinite-Layer Nickelates	7
A. AFM and XRD of Optimized Films	7
B. Reduction Effects on the Film Surface	8
References	11

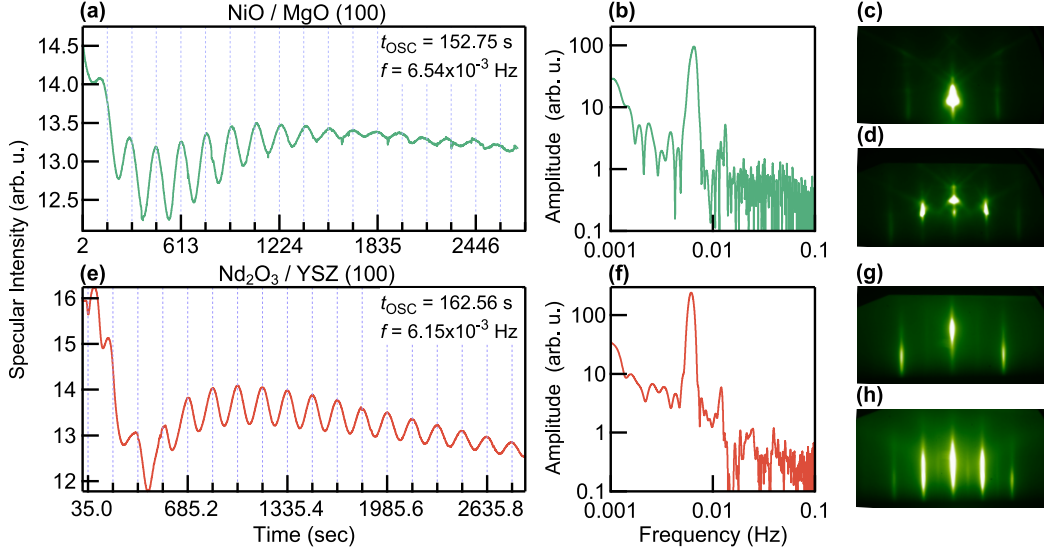


FIG. S1. RHEED Oscillations of the binary oxides NiO/MgO (100) and $\text{Nd}_2\text{O}_3/\text{YSZ}$ (111) used for calibration. (a) RHEED specular intensity of a NiO film during growth. (B) Fourier transform of the specular intensity showing a sharp peak at the monolayer frequency. (c-d) Post-growth RHEED images of the NiO film. (e-h) Same for a representative Nd_2O_3 film.

I. PEROVSKITE NICKELATES

The stoichiometric calibration of nickelate films is of paramount importance to the growth of high-quality NdNiO_3 . As the binary oxide constituents, Nd_2O_3 and NiO have negligible volatility, an absorption-controlled approach in molecular beam epitaxy (MBE) is not possible – excess deposited material either incorporates or forms precipitates – both of which negatively impact the film quality. Studies of the pulsed laser deposition (PLD) and MBE growth of nickelates indicate that deviation from a cation ratio of 1:1 has strong effects on the electrical properties of NdNiO_3 films [1–4] and a strong influence on the quality of subsequently reduced films – particularly the presence of Ruddlesden-Popper (RP) intergrowths [5–7]. In PLD growth, careful control of the film stoichiometry can be achieved through control of the laser fluence and source material (by repolishing the target surface to combat laser-induced changes [2], for instance). In MBE, on the other hand, the key is to establish the elemental source fluxes with a high degree of accuracy. We find that the typical accuracy of a quartz crystal microbalance (QCM), 10-15%, is not sufficient to reproducibly grow high-quality nickelate films; we follow instead a two-step calibration procedure detailed here.

A. RHEED Oscillation Calibration

Initial flux measurements are obtained by monitoring RHEED oscillations during the growths of Nd_2O_3 on $(\text{ZrO}_2)_{0.905}(\text{Y}_2\text{O}_3)_{0.095}$ (111) and NiO on MgO (100) using the parameters outlined in Sun et al. [8]. In Fig. S1 we detail the RHEED oscillation measurements of NiO and Nd_2O_3 in (a-d) and (e-h), respectively. While both compounds grow over a very wide range of conditions (ozone flux, substrate temperature) we find the optimal conditions for RHEED oscillations of NiO are around 450 °C (following an 800 °C vacuum anneal to clean the MgO surface). Conversely, it is preferable to grow Nd_2O_3 at higher temperatures, ~ 970 °C to stabilize the hexagonal structure; though often the first few layers will take on a bixbyite structure, evidenced by a noticeably different oscillation frequency as seen in (e). By monitoring the RHEED specular intensity in (a) and (e) and performing a Fourier transform, (b) and (f), the monolayer formation time can be easily extracted and converted into an elemental flux.

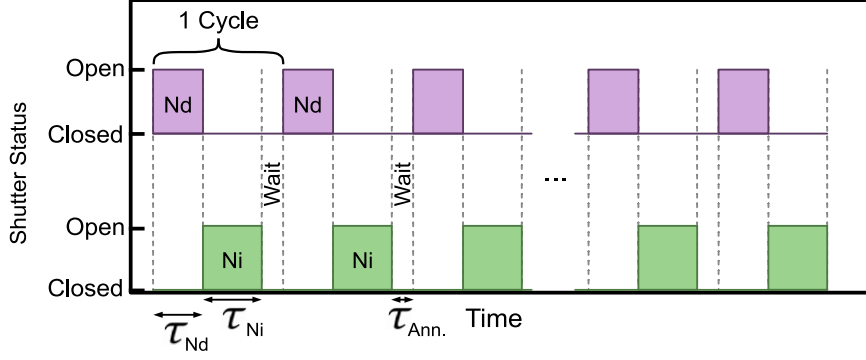


FIG. S2. Shutter timing diagram illustrating the sequential deposition of NdNiO₃ thin films. The shutters for the neodymium and nickel sources are opened in sequence for time periods τ_{Nd} and τ_{Ni} , respectively. Between each cycle the sample is ozone annealed with the shutters closed for a short period of $\tau_{\text{Ann.}} = 5$ seconds to promote full oxidation of the nickel layer, as in Ref. [9].

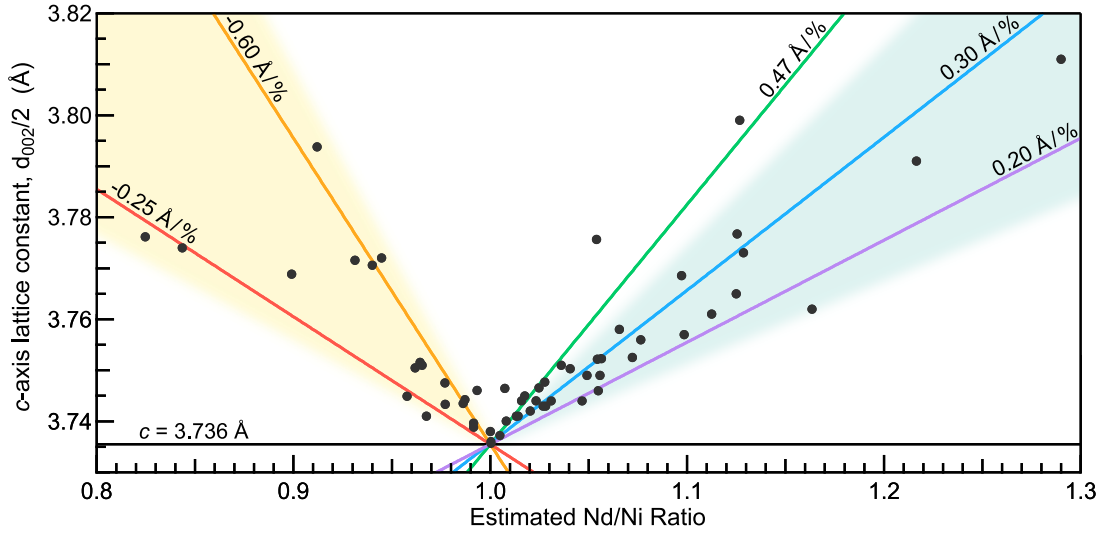


FIG. S3. X-ray diffraction calibration data for 20 u.c. thick films of NdNiO₃ on (001) SrTiO₃. c -axis lattice constant, determined from the 002 peak position, as a function of the nominal cation ratio Nd:Ni. Slopes of typical correction factors employed in the optimization procedure are labeled.

B. XRD and XRR Calibration

While the aforementioned calibration method greatly improves upon the basic calibration using a QCM, we find that its accuracy is typically limited to the few percent scale for each source and as such requires further refinement. This is accomplished using the method described by Li et al. in Ref. 6: the c -axis lattice constant (in our case the 002 peak position) is used as a proxy for non-stoichiometry with the minimal value of the lattice constant corresponding to a stoichiometric cation ratio of Nd:Ni = 1:1. Our repetition of this procedure produces much the same qualitative characteristics as in Ref. [6], although with a slightly lower minimal lattice constant of $c = 3.736 \text{ \AA}$, and is detailed in Fig. S3. To construct this diagram we start by growing a sequence of films with differing shutter times, $\tau_{\text{Nd},\text{Ni}}$, and record the ratio $\tau_{\text{Nd}}/\tau_{\text{Ni}}$. The shutter times τ_{Nd} and τ_{Ni} correspond to our best estimate of the time to deposit a single monolayer of NdO and NiO₂, respectively. A timing diagram showing the sequential opening of the Nd and Ni shutters in a constant background partial pressure of O₃ with a short, 5 second, anneal between cycles is provided in Fig. S2. While the flux ratio $\Phi_{\text{Nd}}/\Phi_{\text{Ni}}$ is not known *a priori*, once the growth sequence converges to near the minimal value this ratio can be calculated from

$$1 = \frac{\Phi_{\text{Nd}}}{\Phi_{\text{Ni}}} \times \frac{\tau_{\text{Nd},f}}{\tau_{\text{Ni},f}}.$$

and applied to the whole sequence to determine the Nd:Ni ratio for all films. Figure S3 is an aggregation of many such growth runs. The scatter increases as we depart from Nd:Ni = 1:1, which is a consequence of source drift on the above procedure. Though modern effusion cells provide excellent flux stability, often reducing flux drift to less than 1% per hour, the difference between $\tau_{\text{Nd}}/\tau_{\text{Ni}}$ at the start of the run and the end (when 1:1 is reached) means that estimation of Nd:Ni for the first samples in the sequence (Nd:Ni \gg 1) is less accurate than at the end (Nd:Ni \sim 1). This estimated cone of uncertainty is illustrated by the shaded regions. Despite this uncertainty in the non-stoichiometry of films well away from 1:1, in the region near the minimum lattice constant discernible changes are still observed down to single percent changes in the shutter times, evidencing that this method can be used to hone the non-stoichiometry down to the percent level or less.

A typical optimization routine at the start of a growth campaign consists of starting with the RHEED oscillation calibration of one or both of Nd and Ni. Then the starting shutter times are calculated to begin with a few percent of excess Neodymium to bias the initial growth towards Nd:Ni $>$ 1; this is to ensure that the direction of the first step is known *a priori* (i.e., reducing the Nd shutter time) and to avoid venturing into the Ni-rich side of the diagram. We find that on the Ni-rich side the relationship between d_{002} and the shutter times is less repeatable. We attribute this to the propensity of excess Ni to precipitate out of the film in the form of NiO, rather than readily incorporating like neodymium does. The flux ratio can then be ‘walked-in’ to 1:1 by progressive adjustment of the shutter times, growth, and XRD measurement. If the starting Nd excess is greater than 10% or so an ‘aggressive’ adjustment factor of 0.2 to 0.3 Å/% can be used in tuning the shutter times between subsequent films; as Nd excess is further reduced more conservative values of 0.3 to 0.47 Å/% are used to avoid accidentally jumping over onto the Ni-rich side. Once the Nd:Ni ratio is within 5-7% of the 1:1 stoichiometric ratio, the total film thickness can also be fine-tuned (by changing τ_{Nd} and τ_{Ni} by the same fraction) to match the desired number of unit cells, typically 20, based on x-ray reflectivity (XRR) measurements of the NdNiO₃ film thickness.

C. Effects of Non-Stoichiometry on Transport

Here we describe the effects of non-stoichiometry on the transport properties of NdNiO₃ films grown on (001) SrTiO₃. The temperature dependent resistivity of a sequence of samples of varying lattice constants (and estimated non-stoichiometry based on Fig. S3) are presented in Fig. S4. The film with the lowest lattice constant has a low room-temperature resistivity of $\sim 200\mu\Omega\text{-cm}$, and a sharp metal-to-insulator transition (MIT) with a jump of nearly two decades. The structural quality is also evident in the accompanying RHEED image, where sharp diffraction peaks are visible on the primary and half-order streaks. As the Nd:Ni ratio is increased a clear increase in the resistivity is visible (up to an order of magnitude), along with a broadening of the MIT and widening of the hysteresis loop. At the same time the sharp diffraction peaks fade and the RHEED streaks become ‘peanut shaped’ – likely due to an increase in the film roughness. We note a marked difference between Nd-rich films under tensile strain when compared to prior measurements under compressive strain [1, 2] where excess Nd drives the films metallic. As previously noted in studies of non-stoichiometry on SrTiO₃ [3] the MIT temperature *increases* with increasing Nd content, and the MIT is not suppressed even up to very high levels (Nd:Ni \sim 1.25). Finally, on the nickel-rich side of the diagram broadening of the MIT and an overall increase of the resistivity are observed. These results indicate that a stoichiometric film on SrTiO₃ is the one with a minimum lattice constant, maximum transition sharpness, and minimum resistivity of the metallic state.

D. Additional Aging Effect Data

In Fig. S5 (unshifted) raw data corresponding to the sample aging study presented in Fig. 2 of the main text. Figs. S5(a) and S5(b) are reproduced from the main text for reference and Figs. S5(c) and S5(d) show data for the sample that was measured at much shorter intervals following growth. It is evident that in both cases a gradual increase of the film resistivity is present over time, with the room temperature values increasing by a factor of 4-5 over the course of ~ 3.5 weeks while stored in a dry, N₂ purged desiccator.

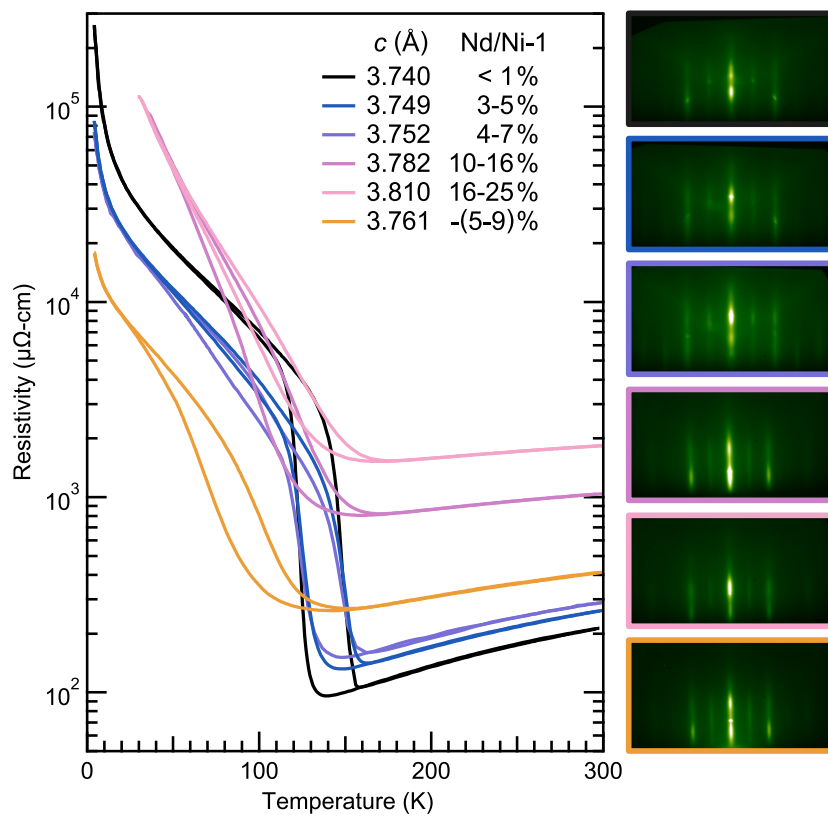


FIG. S4. Effects of cation non-stoichiometry on 20 u.c. thick NdNiO_3 thin films grown on (001)-oriented SrTiO_3 . Resistivity measurements of films of varying non-stoichiometry from slightly nickel rich to highly neodymium rich. Post-growth RHEED images, viewed along the $[110]_{\text{pc}}$ azimuth, of each of the films are pictured on the right. All images use a linear intensity scale.

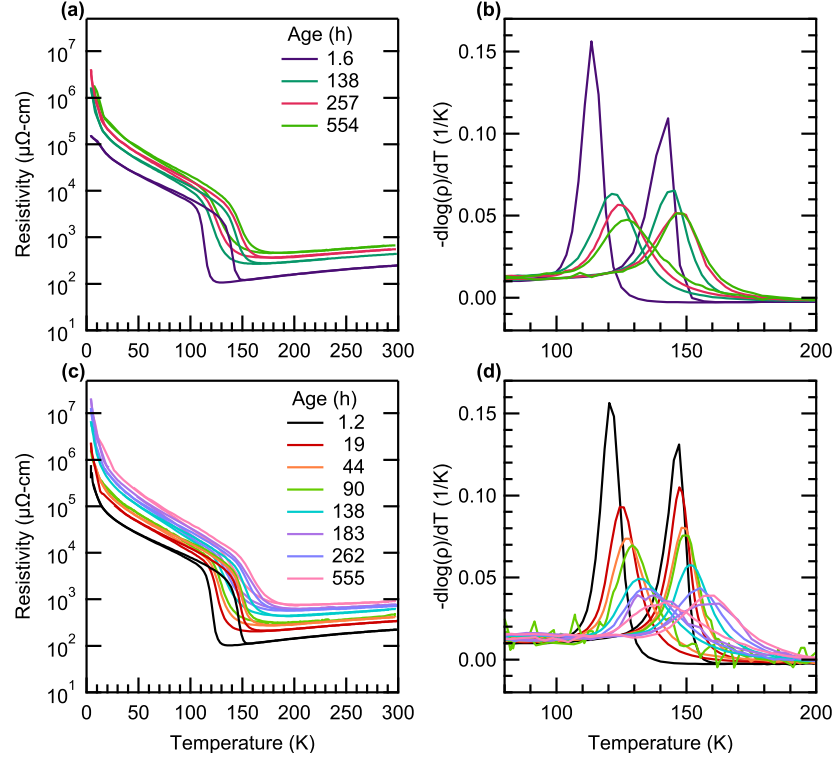


FIG. S5. Aging effects on the transport properties of stoichiometric NdNiO₃ films grown on SrTiO₃. (a) Resistivity of a single NdNiO₃ film measured periodically following growth, reproduced from the main text. (b) Logarithmic derivative of the transport curves in panel (a). (c) Resistivity of another film measured at a higher frequency over the same period of time as the one pictured in panel (a). (d) Logarithmic derivative of the resistivity curves in (c).

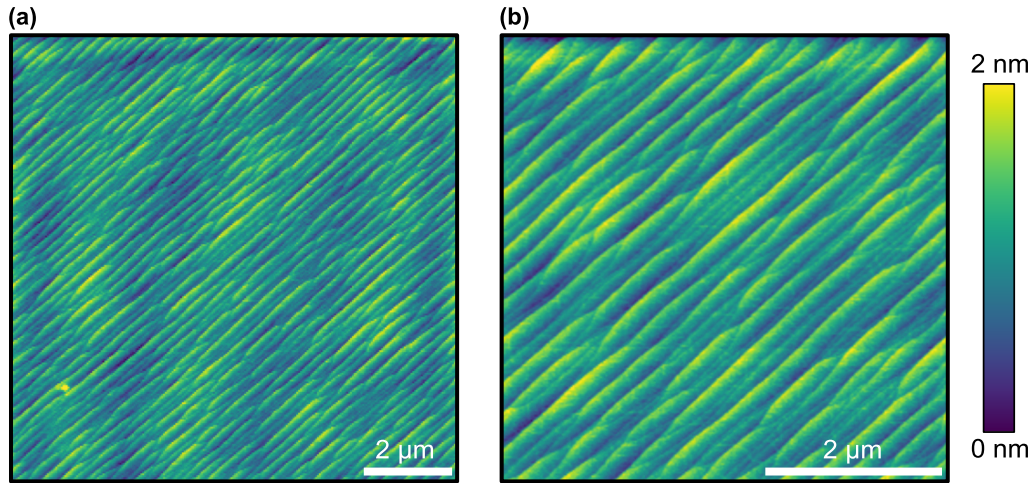


FIG. S6. Larger field of view AFM images of the aged, stoichiometric NdNiO₃ sample shown in Fig. 3(f) of the main text. (a) An AFM image covering a $10 \times 10 \mu\text{m}$ field of view. (b) A $5 \times 5 \mu\text{m}$ field of view where striations running across and through the stepped terraces are visible. A smooth polynomial background has been subtracted from both height profiles to level the images over the wide scan area.

II. INFINITE-LAYER NICKELATES

A. AFM and XRD of Optimized Films

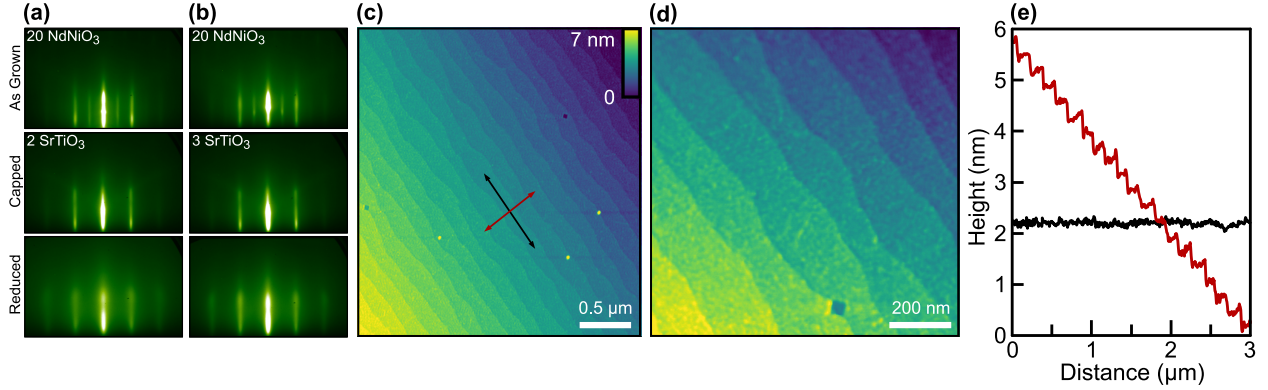


FIG. S7. Measurements of the surface quality of NdNiO_2 films reduced using atomic hydrogen. (a) RHEED images taken along the $[110]_{pc}$ azimuth of an as grown 20 u.c. thick NdNiO_3 film, the same film after capping with 2 u.c. of SrTiO_3 , and after atomic hydrogen reduction. (b) The same as in (a) but with a 3 u.c. thick SrTiO_3 cap. (c) AFM image of a 20 u.c. thick NdNiO_2 film capped with 2 u.c. of SrTiO_3 and reduced with atomic hydrogen; the extracted terrace-averaged RMS roughness is 124 ± 10 pm. (d) Zoom in on the stepped terraces. (e) Line profiles along (black) and across (red) the terraces showing preservation of the substrate's atomic steps. RHEED images in (a) and (b) use a linear intensity scale.

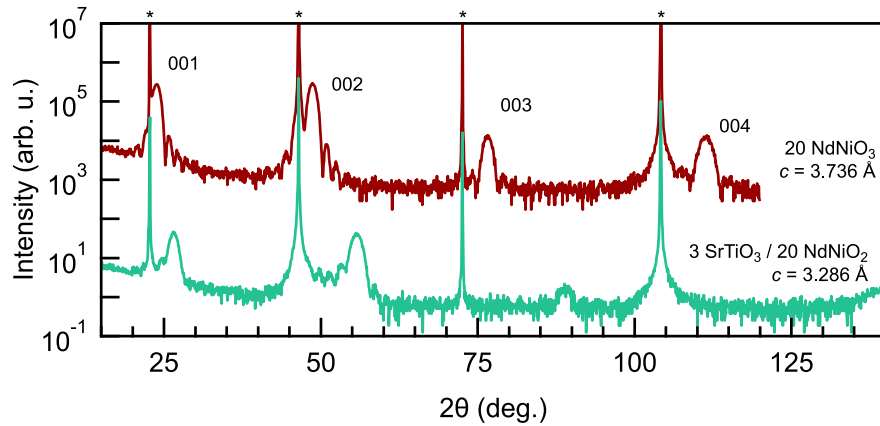


FIG. S8. Diffraction intensity along the specular direction for an uncapped 20 u.c. thick NdNiO_3 film and a 3 u.c. SrTiO_3 capped NdNiO_2 film grown on SrTiO_3 showing the $00L$ reflections. Nelson-Riley analysis of the infinite-layer film peaks gives a lattice constant of $c = 3.286$ Å. (*) indicates reflections from the (001) SrTiO_3 substrate.

In this section we present additional measurements of optimized, reduced NdNiO_2 films on SrTiO_3 . In Fig. S7 we show RHEED images and AFM topography of a reduced infinite-layer films. Figs. S7(a) and S7(b) present RHEED images of additional 20 u.c. thick NdNiO_3 films after growth, after capping, and after atomic hydrogen reduction. In both reduced films, reduced using the optimized three-step procedure, the preservation of the RHEED streaks indicates the film surface remains ordered. The RHEED images of both films are qualitatively similar, though the 3 u.c. capped film appears to have a slightly lower incoherent background than that of the film with the thinner cap. Figures S7(c)-(e) show AFM measurements of a 20 u.c. thick NdNiO_2 film capped with 2 u.c. of SrTiO_3 and reduced with atomic hydrogen. The reduced film shows a stepped terrace structure analogous to the atomically flat substrate on which it was grown, with a low surface roughness of ~ 124 pm. This is similar to films reduced using the solid-state aluminum reduction process introduced in Ref. 10. In Fig. S8 we show larger area $\theta - 2\theta$ scans of a perovskite, NdNiO_3 , film and an optimized, reduced infinite-layer, NdNiO_2 , film which cover all of the $00L$ peaks observable with Cu

K α x-rays. In the infinite-layer film, all four reflections are visible, with the 004 peak sitting at the end of the range accessible with our goniometer.

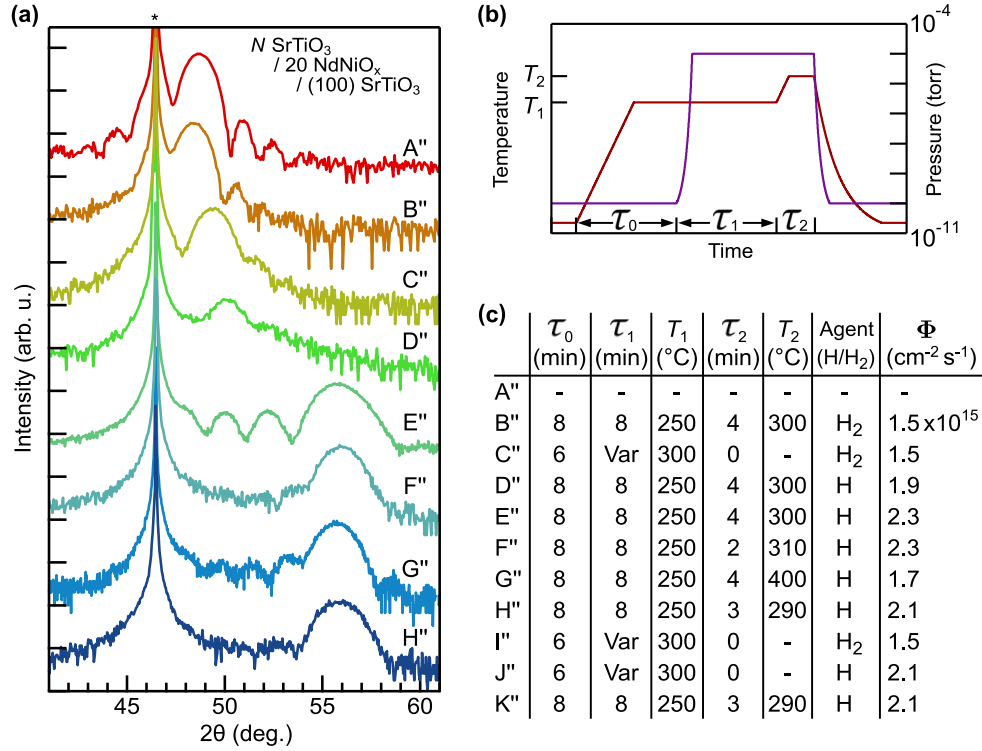


FIG. S9. Conditions used for H and H₂ reduction of films during experiments exploring the effect of the SrTiO₃ cap on reduction. (a) Replica of Fig. 7(a) from the main text with samples labeled. (b) Cartoon of a generic three-step ($\tau_2 \neq 0$) or two-step ($\tau_2 = 0$) reduction. (c) Table of reduction conditions used in the preparation of samples in (a) as well as in Figs. S10, S11, and S12.

B. Reduction Effects on the Film Surface

In this section we present additional data concerning the effects of molecular and atomic hydrogen on the film surface. In Fig. S9 we present the details of the reduction program used for samples in Fig. 7 (samples A''-G'') of the main text as well as those presented later in this section (samples I'', J''). Of these, several samples were subjected to several sequential single-step reduction cycles ($\tau_2 = 0$) with variable times, performing RHEED measurements between cycles. These include sample C'', which was reduced in four increments of 15, 15, 15, and 45 minutes (90 min total), sample I'' in four increments of 15, 30, 30, and 15 minutes (90 min total), and J'' in three increments of 15, 15, and 30 minutes (60 min total). Fluxes are quoted in atoms/cm²/sec for samples reduced with atomic hydrogen and in molecules/cm²/sec for those reduced with molecular hydrogen only. In all cases a consistent hydrogen flow rate of 0.72 sccm was used (giving a chamber pressure of $\sim 9.5 \times 10^{-6}$ torr) and the atomic hydrogen flux was adjusted by tuning the cracker temperature.

In Figs. S10 and S11 we detail two additional progressive annealing experiments. Figure S10 shows a sample with a 2 u.c. thick SrTiO₃ cap annealed in molecular hydrogen. As can be seen in the RHEED images, the molecular hydrogen has little-to-no impact on the SrTiO₃ surface, even for long exposure times. Similar to the uncapped sample shown in the main text, molecular hydrogen is insufficient to produce the infinite-layer phase (under these conditions) and instead an oxygen-deficient perovskite phase is visible in the XRD, with out-of-plane lattice parameter $c \sim 3.69$ Å, following 90 minutes of exposure. Figure S11 shows a sample that was exposed to atomic hydrogen in progressive steps. Similar to the sample presented in the main text, the RHEED images indicate a rapid degradation of the film surface and the presence of other phases (faint rings and additional spots). Even after a relatively long exposure, 60 minutes, the majority of the film remains an oxygen-deficient perovskite ($c \sim 3.69$ Å) without any indication of formation of the infinite-layer phase, evidenced by the XRD patterns in Fig. S11(b).

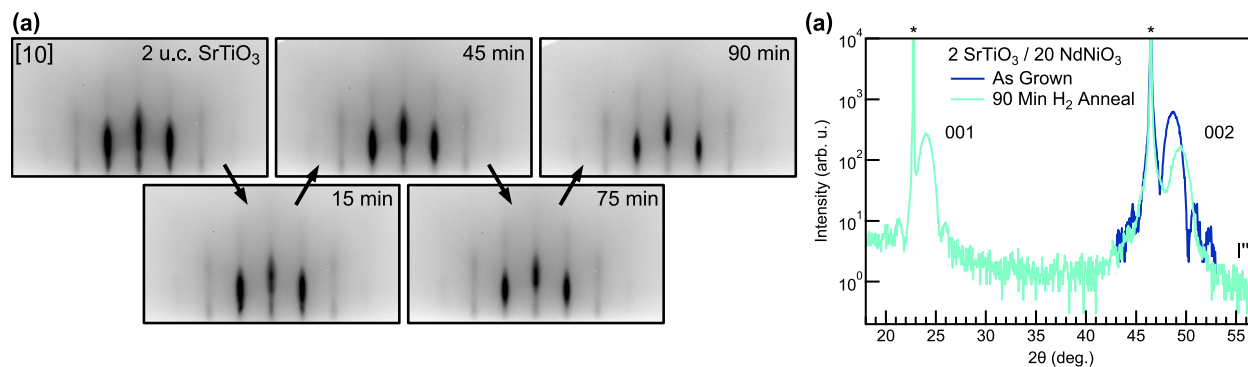


FIG. S10. Molecular hydrogen reduction of a 20 u.c. thick NdNiO₃ / SrTiO₃ film capped with 2 u.c. of SrTiO₃. (a) RHEED images along the [10] azimuth of a film exposed to H₂, at a temperature of 300 °C, for repeated intervals accumulating to 90 minutes total. (b) XRD measurements of the same film before and after the 90 minutes of total reduction time. (*) indicates reflections from the (001) oriented SrTiO₃ substrate.

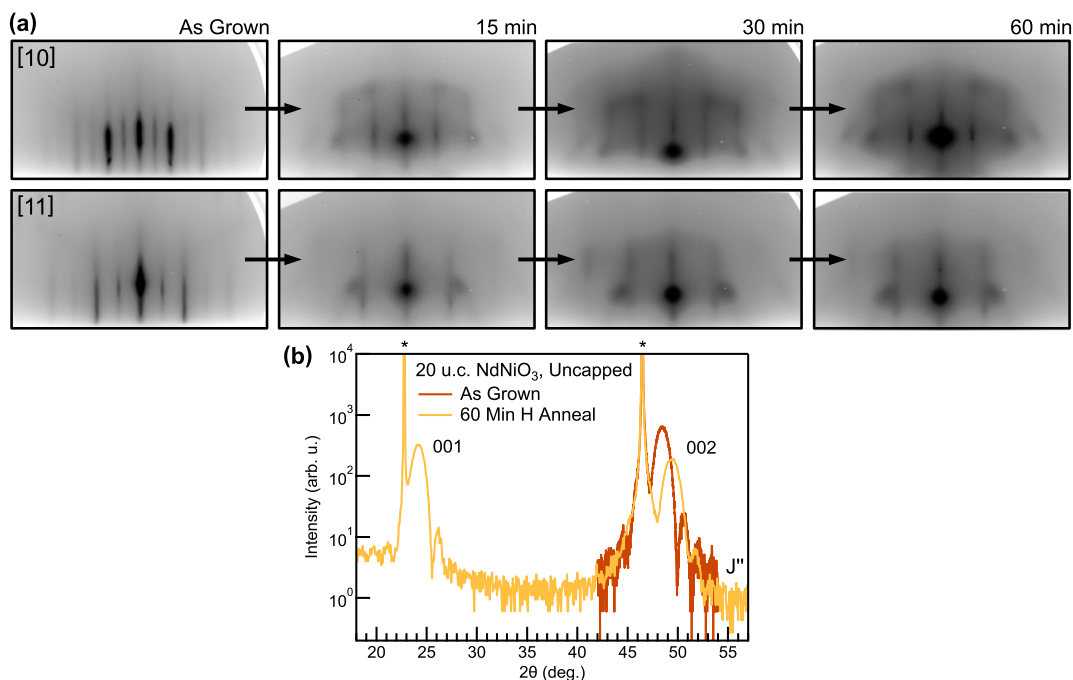


FIG. S11. Effects of atomic hydrogen reduction on an uncapped, 20 u.c. thick NdNiO₃ / SrTiO₃ film. (a) RHEED images along the [100]_{pc} and [110]_{pc} azimuths of an uncapped film; images are taken of the as grown film surface as well as after 15, 30, and 60 minutes of atomic hydrogen exposure time at a sample temperature of 300 °C. (b) XRD measurements of the same film before and after the 60 minute exposure. (*) indicates reflections from the (001) oriented SrTiO₃ substrate.

Finally, we discuss the effects of amorphous capping layers on the reduction of 20 u.c. NdNiO₃/SrTiO₃ films using atomic hydrogen. X-ray diffraction measurements showing the 001 and 002 peak regions for two films with amorphous caps are provided in Fig. S12(a). For both films, the capping layer was deposited in a background pressure of 2×10^{-6} torr of distilled O₃ with the sample at room temperature. For sample H'' the capping layer was deposited with Sr and Ti shutters opened simultaneously (codeposition) and for sample K'' the shutters were opened sequentially (shuttered deposition); in both cases no streaks, spots, or rings were visible in RHEED after deposition of the SrTiO₃ layers. The thickness of both capping layers was 1.2 nm – equivalent to 3 u.c. of SrTiO₃ – and the subsequent reductions, using the same conditions, appear to progress similarly based on the XRD measurements in Fig. S12(a). The obvious difference in XRD patterns between those samples reduced (using atomic hydrogen) with an amorphous cap (H'' and K'') versus those reduced with no cap (D'' and J'') illustrate the importance of the overlayer in facilitating

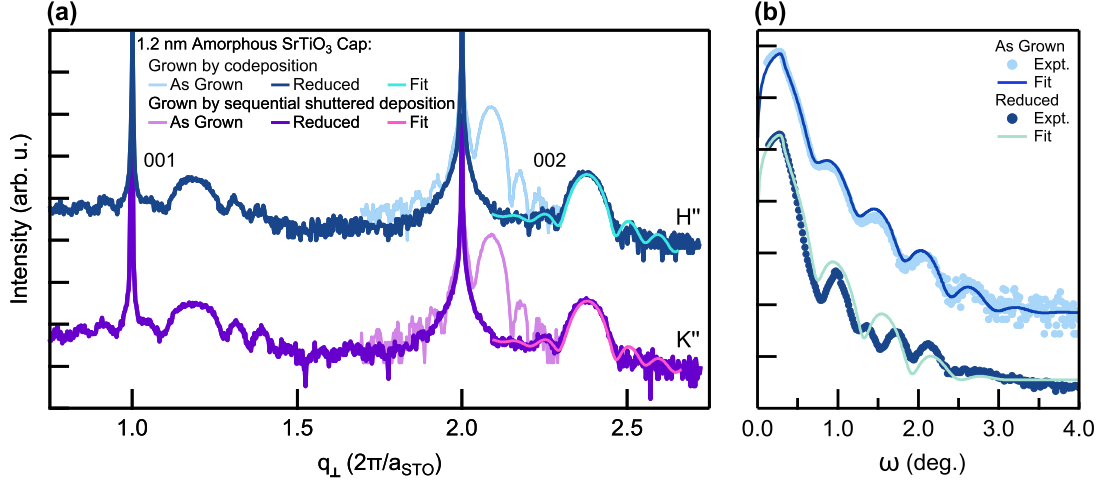


FIG. S12. Atomic hydrogen reduction of 20 u.c. thick $\text{NdNiO}_3 / \text{SrTiO}_3$ films capped with 1.2 nm of amorphous SrTiO_3 . (a) XRD of nickelate films as grown (light) and after capping and reduction (dark); capping layers were grown using either simultaneous codeposition of Sr and Ti (blue) or sequential shuttered deposition (purple) at room temperature. 002 peaks of the reduced films are fit with an N -slit interference pattern (teal, pink) to extract the coherent thickness. (b) Low-angle XRR of one of the samples before and after capping/reduction (dots) and corresponding best fits (lines) using a three slab model.

the reduction even in the absence of epitaxial stabilization.

We do note, however, that the quality of the amorphous SrTiO_3 capped samples are somewhat reduced compared to those with a crystalline cap. Fitting of the XRD patterns of both the reduced films with an N -slit interference pattern,

$$I \propto \frac{1}{N} \frac{\sin^2(Naq/2)}{\sin^2(aq/2)},$$

gives a Scherrer thickness of only 4.43 nm, *i.e.* $N \sim 13.5$, indicating that the coherent crystalline region does not extend across the entirety of the film thickness. Additionally, the x-ray reflectivity, Fig. S12(b), of the reduced film cannot be accurately fit using a three-slab model ($\text{SrTiO}_3/\text{NdNiO}_3/\text{SrTiO}_3$) as was done for the crystalline film in Fig. 5(d) of the main text. The best-fit (green) for this reflectivity curve gives a roughness for the NdNiO_2 layer, 3.2 nm (compared to that of the as grown film, 0.48 nm), and a thickness of 5.6 nm (intermediate to the Scherrer thickness of 4.4 nm and the expected thickness of 6.5 nm). These results are consistent with the capping layer providing some measure of epitaxial support during the reduction process, which is absent in those films with an amorphous cap, and a fraction of the film either forms a defect phase or decomposes – as reported previously in CaH_2 reduced films [5]. We cannot rule out, however, that the observed differences between the crystalline and amorphous SrTiO_3 capped films result from differences in transport of the reactants (*e.g.* H or O_2) through the different matrices. We emphasize, however, that the role of the capping layer, at least in atomic hydrogen reduction experiments, clearly goes beyond that of epitaxial stabilization. In the XRD patterns of uncapped films, D'' and J'', the effect of the reduction is *not* to cause decomposition of the entire thickness of the film, but rather to form a polycrystalline scale on the surface and to hamper further reduction – as evidenced by the minor 002 peak shifts observed in XRD. This is in contrast with the more modest observed differences between crystalline capped (Samples F'', G'') and amorphous capped (Samples H'', K'') films which all exhibit similar 002 peak positions.

-
- [1] E. Breckenfeld, Z. Chen, A. R. Damodaran, and L. W. Martin, Effects of nonequilibrium growth, nonstoichiometry, and film orientation on the metal-to-insulator transition in NdNiO₃ thin films, *ACS Applied Materials and Interfaces* **6**, 22436 (2014).
- [2] D. Preziosi, A. Sander, A. Barthélémy, and M. Bibes, Reproducibility and off-stoichiometry issues in nickelate thin films grown by pulsed laser deposition, *AIP Advances* **7**, 015210 (2017).
- [3] T. Yamanaka, A. N. Hattori, L. N. Pamasi, S. Takemoto, K. Hattori, H. Daimon, K. Sato, and H. Tanaka, Effects of Off-Stoichiometry in the Epitaxial NdNiO₃ Film on the Suppression of Its Metal-Insulator-Transition Properties, *ACS Applied Electronic Materials* **1**, 2678 (2019).
- [4] G. A. Pan, Q. Song, D. Ferenc Segedin, M. C. Jung, H. El-Sherif, E. E. Fleck, B. H. Goodge, S. Doyle, D. Córdova Carrizales, A. T. N'Diaye, P. Shafer, H. Paik, L. F. Kourkoutis, I. El Baggari, A. S. Botana, C. M. Brooks, and J. A. Mundy, Synthesis and electronic properties of Nd_{n+1}Ni_nO_{3n+1} Ruddlesden-Popper nickelate thin films, *Physical Review Materials* **6**, 055003 (2022).
- [5] K. Lee, B. H. Goodge, D. Li, M. Osada, B. Y. Wang, Y. Cui, L. F. Kourkoutis, and H. Y. Hwang, Aspects of the synthesis of thin film superconducting infinite-layer nickelates, *APL Materials* **8**, 041107 (2020).
- [6] Y. Li, W. Sun, J. Yang, X. Cai, W. Guo, Z. Gu, Y. Zhu, and Y. Nie, Impact of Cation Stoichiometry on the Crystalline Structure and Superconductivity in Nickelates, *Frontiers in Physics* **9**, 1 (2021).
- [7] K. Lee, B. Y. Wang, M. Osada, B. H. Goodge, T. C. Wang, Y. Lee, S. Harvey, W. J. Kim, Y. Yu, C. Murthy, S. Raghu, L. F. Kourkoutis, and H. Y. Hwang, Linear-in-temperature resistivity for optimally superconducting (Nd,Sr)NiO₂, *Nature* **619**, 288 (2023).
- [8] J. Sun, C. T. Parzyck, J. H. Lee, C. M. Brooks, L. F. Kourkoutis, X. Ke, R. Misra, J. Schubert, F. V. Hensling, M. R. Barone, Z. Wang, M. E. Holtz, N. J. Schreiber, Q. Song, H. Paik, T. Heeg, D. A. Muller, K. M. Shen, and D. G. Schlom, Canonical approach to cation flux calibration in oxide molecular-beam epitaxy, *Physical Review Materials* **6**, 033802 (2022).
- [9] P. D. C. King, H. I. Wei, Y. F. Nie, M. Uchida, C. Adamo, S. Zhu, X. He, I. Božović, D. G. Schlom, and K. M. Shen, Atomic-scale control of competing electronic phases in ultrathin LaNiO₃, *Nature Nanotechnology* **9**, 443 (2014).
- [10] W. Wei, K. Shin, H. Hong, Y. Shin, A. S. Thind, Y. Yang, R. F. Klie, F. J. Walker, and C. H. Ahn, Solid state reduction of nickelate thin films, *Physical Review Materials* **7**, 013802 (2023).